

## IMMUNOLOGY

# IRF3 inhibits inflammatory signaling pathways in macrophages to prevent viral pathogenesis

Sukanya Chakravarty<sup>1,2</sup>, Merina Varghese<sup>1</sup>, Shumin Fan<sup>1</sup>, Roger Travis Taylor<sup>1</sup>, Ritu Chakravarti<sup>3</sup>, Saurabh Chattopadhyay<sup>1,2\*</sup>

Viral inflammation contributes to pathogenesis and mortality during respiratory virus infections. IRF3, a critical component of innate antiviral immune responses, interacts with pro-inflammatory transcription factor NF-κB, and inhibits its activity. This mechanism helps suppress inflammatory gene expression in virus-infected cells and mice. We evaluated the cells responsible for IRF3-mediated suppression of viral inflammation using newly engineered conditional *Irf3*<sup>Δ/Δ</sup> mice. *Irf3*<sup>Δ/Δ</sup> mice, upon respiratory virus infection, showed increased susceptibility and mortality. *Irf3* deficiency caused enhanced inflammatory gene expression, lung inflammation, immunopathology, and damage, accompanied by increased infiltration of pro-inflammatory macrophages. Deletion of *Irf3* in macrophages (*Irf3*<sup>MKO</sup>) displayed, similar to *Irf3*<sup>Δ/Δ</sup> mice, increased inflammatory responses, macrophage infiltration, lung damage, and lethality, indicating that IRF3 in these cells suppressed lung inflammation. RNA-seq analyses revealed enhanced NF-κB-dependent gene expression along with activation of inflammatory signaling pathways in infected *Irf3*<sup>MKO</sup> lungs. Targeted analyses revealed activated MAPK signaling in *Irf3*<sup>MKO</sup> lungs. Therefore, IRF3 inhibited inflammatory signaling pathways in macrophages to prevent viral inflammation and pathogenesis.

Copyright © 2024 The Authors, some rights reserved; exclusive licensee American Association for the Advancement of Science. No claim to original U.S. Government Works. Distributed under a Creative Commons Attribution NonCommercial License 4.0 (CC BY-NC).

## INTRODUCTION

Respiratory viruses—e.g., influenza A virus, respiratory syncytial virus, and coronavirus (CoV)—are major causative agents for morbidity and mortality in humans (1–5). In recent years, COVID-19, caused by a member of CoV, severe acute respiratory syndrome CoV 2 (SARS-CoV-2), led to extensive damage globally. Respiratory viruses infect primarily lung cells and cause lung injury; however, the resulting inflammation can often dissipate throughout the body, damaging secondary organs, e.g., the heart and the brain (6–8). Lung tissue has a highly heterogeneous structure, composed of both immune and nonimmune cells; airway epithelial cells (AECs), as well as endothelial cells, provide the early sites for respiratory virus infection (9, 10). Initial replication in these cells results in increased lung viral load, which triggers the production of inflammatory cytokines. Cytokines are secreted and help recruit immune cells—e.g., neutrophils, macrophages, dendritic cells, and natural killer cells—to infected lungs (11–13). These immune cells are critical mediators in resolving infection by amplifying cytokine production, causing lung inflammation, a host defense strategy. However, excessive production of cytokines, a common phenomenon in uncontrolled respiratory infection, leads to acute respiratory distress syndrome, severe lung damage, and host mortality.

Innate immunity is the first line of host defense against virus infections. Virus infection is sensed by cellular pattern recognition receptors (PRRs), such as Toll-like receptors (TLRs), RIG-I-like receptors, cyclic guanosine 5'-monophosphate–adenosine 5'-monophosphate synthase, which detect pathogen-associated molecular patterns (PAMPs) (14, 15). PAMP recognition activates PRRs, which signal through intracellular adaptor proteins, e.g., TRIF, MyD88, MAVS, and STING, to activate Ser/Thr kinases, e.g., TANK-binding kinase 1 and IκB kinase ε (IKKε), which directly phosphorylate the inactive transcription

factors such as interferon regulatory factor 3 (IRF3) (16). Phosphorylated IRF3 gets dimerized and translocated into the nucleus to induce antiviral genes, e.g., interferons (IFNs) and IFN-stimulated genes (ISGs) (17). Many ISGs act as viral restriction factors by interfering with specific stages of viral life cycle to inhibit viral replication (18, 19). In addition to IRF3, PRRs also activate IKK, which phosphorylates IκBα, leading to its proteasomal degradation and thus activating nuclear factor κB (NF-κB), a pro-inflammatory transcription factor. Activated NF-κB then translocates to the nucleus to induce genes responsible for inflammatory cytokines (15, 20). IFN-β, a critical antiviral cytokine produced by the virus-infected cells, requires cooperative action of IRF3 and NF-κB. The strength, balance, and duration of antiviral (IRF3-mediated) and inflammatory (NF-κB-mediated) signaling pathways determine the outcome of virus infection (21).

*Irf3*, expressed ubiquitously, is an essential transcription factor, which gets activated rapidly in the virus-infected cells for inducing IFN-β. *Irf3* deficiency, as a result, leads to increased viral replication and lethality. In addition to its canonical transcriptional role, we uncovered noncanonical functions of IRF3 that are independent of its transcriptional activation. IRF3 activates a pro-apoptotic pathway, in which it functions as a chaperone by interacting with and activating a pro-apoptotic protein, BAX. IRF3-BAX complex translocates to mitochondria, leading to the activation of intrinsic apoptotic pathway, RIG-I-like receptor-induced IRF3-mediated pathway of apoptosis (RIPA) (22–24). In contrast to phosphorylation-mediated activation for transcriptional functions, IRF3 is activated by polyubiquitination in virus-infected cells, enabling it to interact with BAX to activate RIPA (22). Knock-in mice—expressing a mutant IRF3, inactive in transcriptional functions but active in RIPA—are protected from respiratory virus infection. The pro-apoptotic activity of IRF3, early during infection, helps eliminate virus-infected cells and functions as an antiviral mechanism of the host. Recently, we uncovered that IRF3, independent of its transcriptional and pro-apoptotic activities, inhibits NF-κB functions (25, 26). For this function, IRF3 interacts directly with NF-κB-p65 subunit; specific domains of both proteins were mapped to identify the interacting interface between IRF3 and NF-κB. As a result of this interaction, IRF3

<sup>1</sup>Department of Medical Microbiology and Immunology, University of Toledo College of Medicine and Life Science, Toledo, OH, USA. <sup>2</sup>Department of Microbiology, Immunology, and Molecular Genetics, University of Kentucky College of Medicine, Lexington, KY, USA. <sup>3</sup>Department of Physiology and Pharmacology, University of Toledo College of Medicine and Life Science, Toledo, OH, USA.  
\*Corresponding author. Email: saurabh.chattpadhyay@uky.edu

inhibits nuclear translocation of NF- $\kappa$ B by sequestering it in cytosol and inhibits NF- $\kappa$ B-dependent gene expression. IRF3 mutants, defective in transcriptional or pro-apoptotic functions, interact with and inhibit NF- $\kappa$ B activity. The new function of IRF3, repression of IRF3-mediated NF- $\kappa$ B activity (RIKA), can suppress NF- $\kappa$ B-mediated inflammatory gene expression in cells and mice. Recently, we expanded the anti-inflammatory function of IRFs to IRF7, which shares IRF3's NF- $\kappa$ B-binding motif and, as a result, can suppress inflammatory gene expression in virus-infected cells (27). It is, therefore, an emerging theme that IRFs contribute to the overall antiviral responses of the host by using different activities, presumably kinetically and cell specifically.

In the current study, we aimed to determine the cell types in which the anti-inflammatory activity of IRF3, RIKA, is responsible for preventing viral inflammation and pathogenesis. Viral inflammation, in addition to viral load, is a major determinant of pathogenesis, and uncontrolled inflammatory responses are detrimental to the host. Using newly engineered mice, expressing floxed (*fl*) *Irf3*, we investigated the cell type-specific role of IRF3 and its different functions against respiratory viral infection. Using Sendai virus (SeV), a model paramyxovirus, and murine hepatitis virus (MHV), a model murine CoV, as respiratory infection models, we identified a critical role of macrophage-specific IRF3 in preventing lung inflammation and, subsequently, viral pathogenesis. The conditional deletion of *Irf3* from macrophages led to the accumulation of pro-inflammatory macrophages and elevated levels of

lung inflammatory genes, which together contributed to increased respiratory pathogenesis. Our results, obtained from a combination of genetic, transcriptomic, and biochemical approaches, therefore illuminate a protective macrophage-specific anti-inflammatory function of IRF3 in preventing viral lung inflammation.

## RESULTS

### IRF3 protects against intranasal SeV and MHV infection in mice

We have shown, using ectopically expressed IRF3 and its mutants in various human and mouse cells, that IRF3 can suppress inflammatory gene expression by interacting with NF- $\kappa$ B (26). Here, we expanded the phenomenon using nontransformed mouse embryonic fibroblasts (MEFs), derived from *Irf3*<sup>WT/WT</sup>, *Irf3*<sup>-/-</sup>, or *Irf3*<sup>S1/S1</sup> mice (22). *Irf3*<sup>-/-</sup> MEFs, upon SeV infection, triggered the enhanced expression of NF- $\kappa$ B-dependent *Tnfaip3* gene compared to *Irf3*<sup>WT/WT</sup> MEFs (fig. S1A). *Irf3*<sup>S1/S1</sup> MEFs, as expected, suppressed the induction of *Tnfaip3*, indicating that RIKA is independent of the transcriptional activity of IRF3. As expected, upon SeV infection, *Irf3*<sup>WT/WT</sup> MEFs, but not *Irf3*<sup>-/-</sup> or *Irf3*<sup>S1/S1</sup> MEFs, induced *Ifnb1*, the IRF3 target gene (fig. S1B). To evaluate the relative contribution of RIKA to the overall antiviral responses of IRF3, we engineered mice expressing *Irf3*, with exons 3 to 6 flanked by loxP sites (*Irf3*<sup>fl/fl</sup>; Fig 1A). *Irf3*<sup>fl/fl</sup> mice are advantageous over the

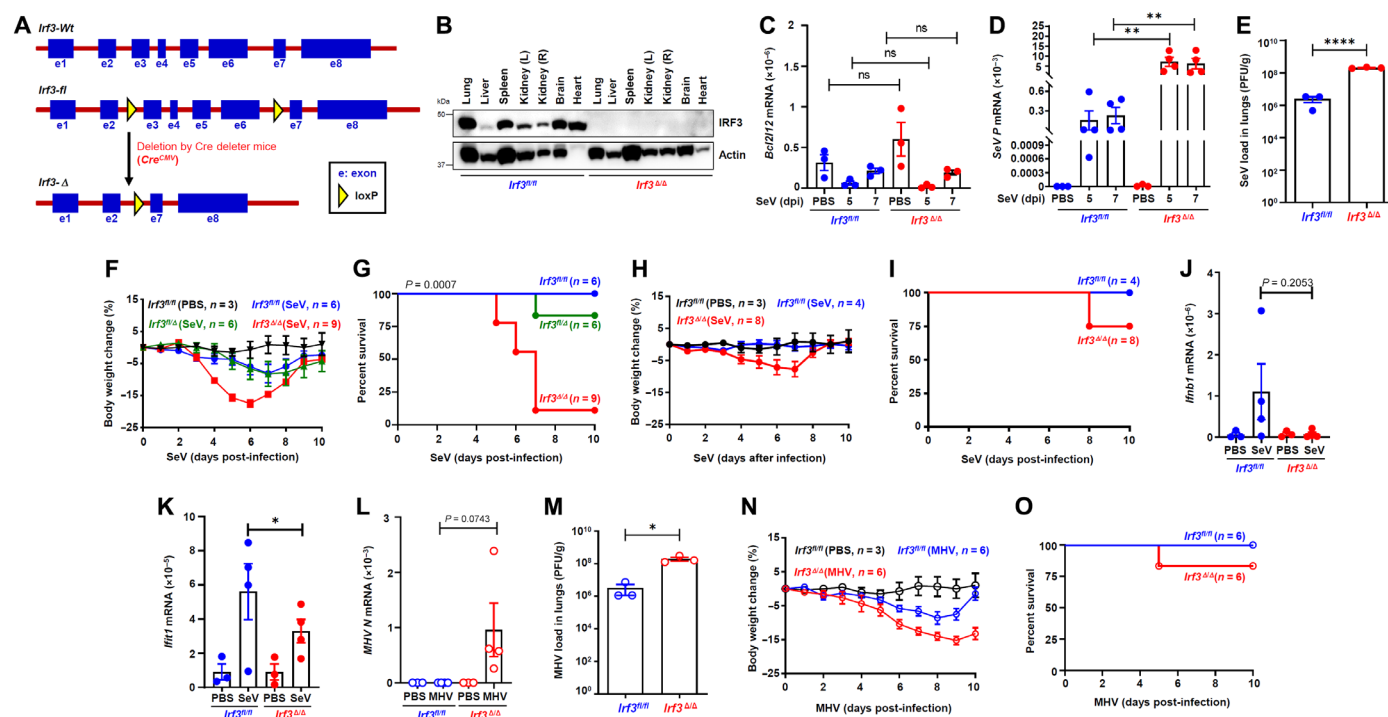


**Fig. 1. Conditional *Irf3* knockout mice are susceptible to respiratory pathogenesis upon SeV and MHV infection.** (A) A schematic showing *Irf3*-Wt, *Irf3*-fl (*Irf3*<sup>fl/fl</sup>), and the derived *Irf3*- $\Delta$  (*Irf3*<sup>Δ/Δ</sup>) mice. (B) Organs from *Irf3*<sup>fl/fl</sup> and *Irf3*<sup>Δ/Δ</sup> mice, upon intranasal SeV [425,000 plaque-forming units (PFU) per mouse] infection, were homogenized and analyzed for IRF3 by immunoblot. (C to K) Mice, as indicated, were either mock-infected [phosphate-buffered saline (PBS)] or infected intranasally with SeV [425,000 PFU per mouse for (C) to (G), and 125,000 PFU per mouse for (H) to (K)] and used for the following analyses: relative expression of *Bcl2l12* (C) and viral mRNA expression (D) by quantitative reverse transcription polymerase chain reaction (qRT-PCR) in the infected lungs, lung SeV infectious particle load by plaque assay (E), body weight changes and survival after viral infection [(F) to (I)], and *Ifnb1* and *Ifit1* mRNA levels by qRT-PCR [(J) and (K)]. (L to O) Indicated mice were either mock-infected (PBS) or infected with MHV ( $10^6$  PFU per mouse) and analyzed for lung viral mRNA expression by qRT-PCR (L), lung MHV infectious virus load by plaque assay (M), body weight changes (N), and survival (O). The results are representatives of at least two to three experiments. The data represent means  $\pm$  SEM;  $n = 3$  to 4, or as indicated, where applicable, each dot represents one mouse and is an average of the three technical replicates. \* $P < 0.05$ , \*\* $P < 0.005$ , and \*\*\* $P < 0.0001$ ; ns, nonsignificant; dpi, days postinfection.

complete *Irf3* knockout mice because (i) *Irf3* gene can be conditionally deleted by inducible *Cre* recombinase at any stage of life, (ii) *Irf3* gene can be deleted in specific cell types by crossing with cell-specific *Cre* recombinase, and (iii) *Irf3<sup>f/f</sup>* mice, unlike previously used *Irf3* knockout mice (22, 26), do not have unexpected deletion of neighboring genes, e.g., *Bcl2l12*. *Irf3<sup>f/f</sup>* mice were crossed with mice expressing *Cre* by a cytomegalovirus (CMV) promoter (*Cre<sup>CMV</sup>*) to generate the complete deletion of *Irf3* from all cells (*Irf3<sup>Δ/Δ</sup>*) (Fig. 1A and fig. S1C). The absence of IRF3 protein was confirmed by immunoblot analyses of tissues isolated from *Irf3<sup>f/f</sup>* and *Irf3<sup>Δ/Δ</sup>* mice (Fig. 1B). These newly derived *Irf3<sup>Δ/Δ</sup>* mice had no deletion of *Bcl2l12* gene, which was expressed at comparable levels in either uninfected or infected *Irf3<sup>f/f</sup>* and *Irf3<sup>Δ/Δ</sup>* mouse lungs (Fig. 1C). The expression of IRF7, a related IRF, remained unaltered in *Irf3<sup>Δ/Δ</sup>* mice (fig. S1D). Intranasal SeV infection, as expected, led to enhanced viral load in *Irf3<sup>Δ/Δ</sup>* mouse lungs, analyzed by viral RNA levels at two different times after infection (Fig. 1D and fig. S1E) and infectious viral load in the lungs (Fig. 1E). Pathogenesis studies revealed that *Irf3<sup>Δ/Δ</sup>* mice were highly susceptible to SeV-induced body weight loss and morbidity, examined at two different doses (Fig. 1, F to I). Heterozygote mice (*Irf3<sup>f/Δ</sup>*), however, showed substantial protection against SeV infection (Fig. 1, F and G). Expectedly, *Irf3<sup>Δ/Δ</sup>* mice,

compared to *Irf3<sup>f/f</sup>* mice, expressed relatively lower levels of *Ifn* genes (Fig 1J and fig. S1F) and IFN-stimulated gene, *Ifit1* (Fig. 1K). We further tested the *Irf3<sup>Δ/Δ</sup>* mice using MHV infection, which causes respiratory pathogenesis upon intranasal administration (28–30). MHV infection led to enhanced lung viral load (Fig. 1, L and M), body weight loss (Fig. 1N), and morbidity (Fig. 1O) in *Irf3<sup>Δ/Δ</sup>* mice compared to *Irf3<sup>f/f</sup>* mice. Overall, conditional *Irf3* deletion caused enhanced viral pathogenesis upon SeV and MHV infection, and *Bcl2l12* had no impact on the increased viral pathogenesis in *Irf3<sup>Δ/Δ</sup>* mice.

### IRF3 prevents respiratory viral pathogenesis by suppressing lung inflammation

Lung inflammation, in addition to enhanced viral load, is a major contributor to respiratory viral pathogenesis (1, 6). We evaluated whether lethality of *Irf3<sup>Δ/Δ</sup>* mice was due to enhanced lung inflammatory responses. Lung immunopathology, analyzed by hematoxylin and eosin (H&E) staining of virus-infected lung sections, revealed enhanced tissue damage in SeV-infected *Irf3<sup>Δ/Δ</sup>* mice (Fig. 2, A and B, and fig. S2A). Inflammatory mediators, e.g., cytokines, are the major drivers of lung inflammation; SeV-infected *Irf3<sup>Δ/Δ</sup>* mice produced higher levels of interleukin-1β (IL-1β) protein in lung homogenates (Fig. 2C and

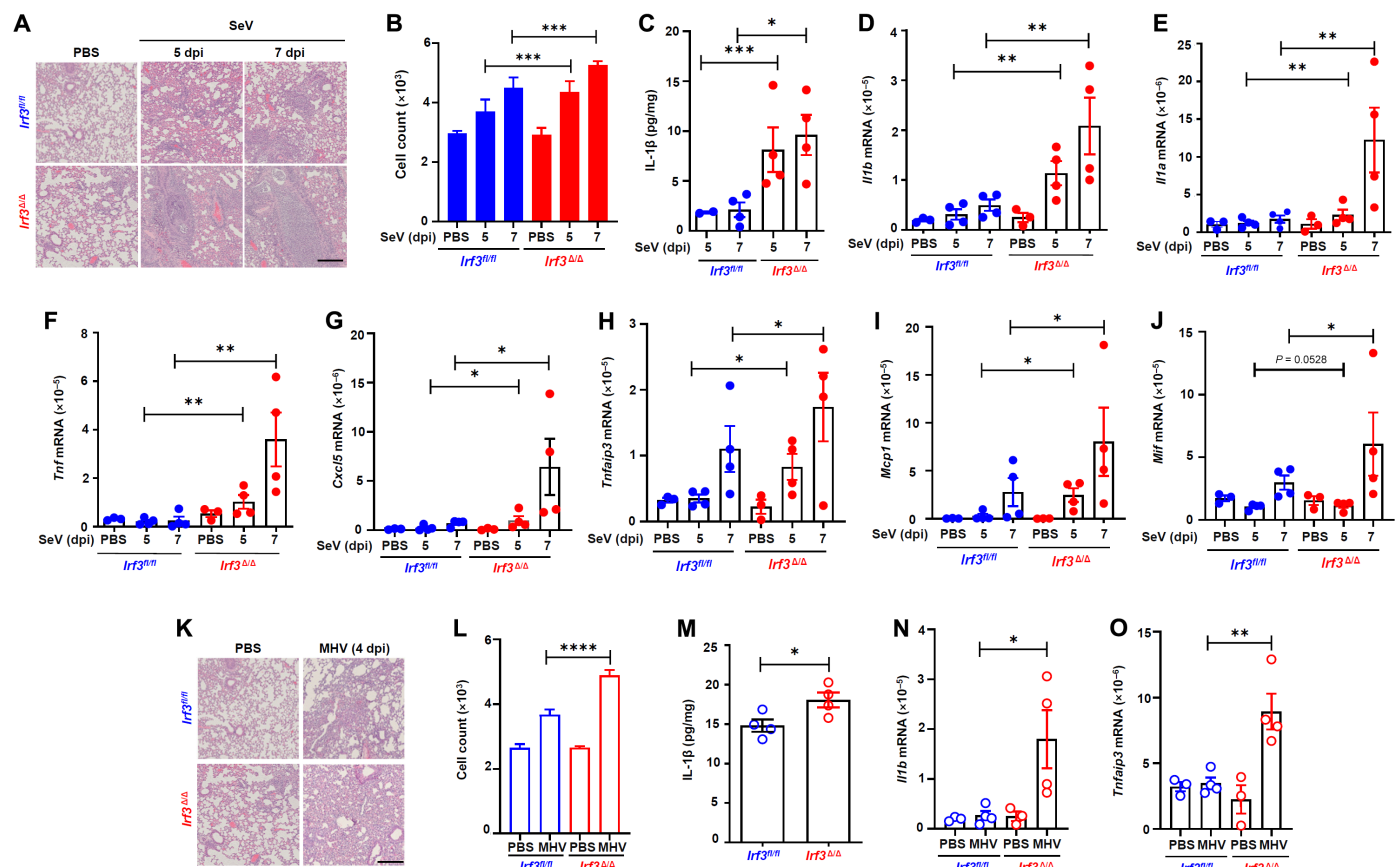


**Fig. 2. Increased lung immunopathology and inflammatory gene expression in *Irf3<sup>Δ/Δ</sup>* mice upon SeV and MHV infection.** (A) to (J) *Irf3<sup>f/f</sup>* and *Irf3<sup>Δ/Δ</sup>* mice were either mock (PBS) or SeV-infected (425,000 PFU per mouse), and the following analyses were performed: H&E staining of mock (PBS) or SeV-infected lung sections (A), quantification of H&E-stained sections (two to three fields per lung section of two mice) (B), IL-1β expression in lung homogenates by enzyme-linked immunosorbent assay (ELISA) (C), relative expression of lung inflammatory target genes (as indicated) by qRT-PCR [(D) to (J)]. (K) to (O) *Irf3<sup>f/f</sup>* and *Irf3<sup>Δ/Δ</sup>* mice were intranasally infected with MHV (10<sup>6</sup> PFU per mouse), and the following analyses were performed: H&E staining of mock (PBS) or MHV-infected lung sections (K), quantification of multiple fields of H&E stained sections from two to three mice (L), and lung inflammatory target genes (as indicated) by ELISA (M) or qRT-PCR (N and O). The results are representatives of at least two to three independent experiments. The data represent means  $\pm$  SEM;  $n = 2$  to 4, where applicable, each dot represents one mouse and is an average of the three technical replicates. \* $P < 0.05$ , \*\* $P < 0.005$ , \*\*\* $P < 0.0005$ , and \*\*\*\* $P < 0.0001$ . Scale bars, 200  $\mu$ m [(A) and (K)].

fig. S2B). *Irf3<sup>Δ/Δ</sup>* mice, in addition to IL-1 $\beta$  protein levels, displayed significantly enhanced mRNA levels of inflammatory genes, e.g., *Il1b*, *Il1a*, *Tnf*, *Cxcl5*, and *Tnfaip3* (Fig. 2, D to H). Chemokines are small proteins secreted by injured tissues, resulting in migration and recruitment of inflammatory cells to the tissue, thereby amplifying inflammation (31, 32). H&E staining indicated infiltration of cells (Fig. 2, A and B, and fig. S2A), leading us to analyze mRNA levels of chemokines, such as *Mcp1* (also known as *Ccl2*) and *Mif* (33, 34). Both chemokines showed enhanced mRNA expression in the lungs of infected *Irf3<sup>Δ/Δ</sup>* mice (Fig. 2, I and J). Similar lung immunopathology was observed by histological analyses of MHV-infected *Irf3<sup>Δ/Δ</sup>* mice (Fig. 2, K and L, and fig. S2C). Lung immunopathology in MHV-infected *Irf3<sup>Δ/Δ</sup>* mice was accompanied by enhanced IL-1 $\beta$  protein levels (Fig. 2M), as well as *Il1b* and *Tnfaip3* mRNA levels (Fig. 2, N and O). Together, increased lethality in *Irf3<sup>Δ/Δ</sup>* mice by respiratory viral infection was accompanied by lung inflammation and injury.

## IRF3 inhibits macrophage infiltration to virus-infected lungs

Virus infection triggers infiltration of immune cells to the site of infection, as observed by H&E staining of SeV and MHV-infected lungs (Fig. 2, A and K, and fig. S2, A and C). Immune cells, e.g., tissue-resident macrophages, play a protective role initially by producing inflammatory cytokines, which, however, lead to infiltration of additional macrophages, causing inflammation-induced tissue injury (2, 35). *Irf3<sup>Δ/Δ</sup>* primary bone marrow-derived macrophages (BMDMs) expressed elevated levels of inflammatory genes (*Il1b*, *Tnf*, and *Tnfaip3*) upon SeV and MHV infection (Fig. 3, A, C, and D). The expression of *Ifnb1*, as expected, was inhibited in *Irf3<sup>Δ/Δ</sup>* BMDMs (Fig. 3, B and E). Because IRF3 inhibited inflammatory gene expression in primary macrophages, we hypothesized that lethal lung inflammation in *Irf3<sup>Δ/Δ</sup>* mice was mediated partly by macrophages. Macrophage markers—e.g., *Cd45*, *F4/80*, and *Cd68*—analyzed by their mRNA levels, were significantly increased in SeV-infected *Irf3<sup>Δ/Δ</sup>* lungs (Fig. 3, F to H). T cell markers, *Cd4* and

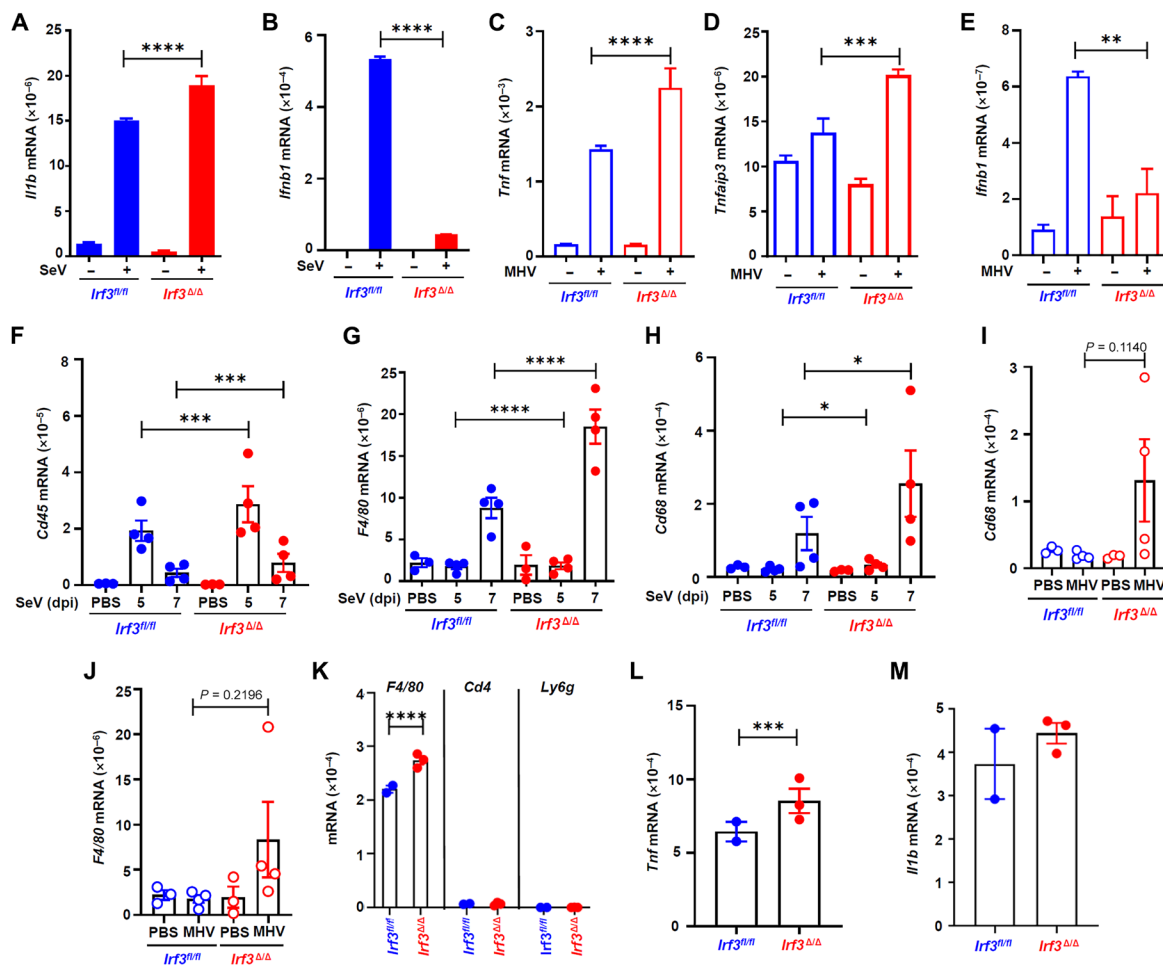


**Fig. 3. Increased macrophage population in *Irf3<sup>Δ/Δ</sup>* lungs upon SeV and MHV infection.** (A and B) Primary BMDMs from *Irf3<sup>fl/fl</sup>* and *Irf3<sup>Δ/Δ</sup>* mice were infected with SeV [Cantell strain, multiplicity of infection (MOI): 5], and *Il1b* and *Ifnb1* mRNA levels were analyzed by qRT-PCR. (C to E) Primary BMDMs from *Irf3<sup>fl/fl</sup>* and *Irf3<sup>Δ/Δ</sup>* mice were infected with MHV (MOI: 5), and *Tnf*, *Tnfaip3*, and *Ifnb1* mRNA levels were analyzed by qRT-PCR. (F to H) *Irf3<sup>fl/fl</sup>* and *Irf3<sup>Δ/Δ</sup>* mice were intranasally infected with SeV (425,000 PFU per mouse), and the lung expression of *Cd45*, *F4/80*, and *Cd68* mRNAs was analyzed by qRT-PCR. (I and J) *Irf3<sup>fl/fl</sup>* and *Irf3<sup>Δ/Δ</sup>* mice were intranasally infected with MHV (10<sup>6</sup> PFU per mouse), and the lung expression of *Cd68* and *F4/80* mRNAs was analyzed by qRT-PCR. (K) Single-cell suspension from SeV-infected *Irf3<sup>fl/fl</sup>* and *Irf3<sup>Δ/Δ</sup>* mouse lungs were pulled down with anti-*F4/80* antibody, and the levels of *F4/80*, *Cd4*, or *Ly6g* mRNAs were analyzed by qRT-PCR. (L and M) Anti-*F4/80* pull down of single-cell suspension from SeV-infected *Irf3<sup>fl/fl</sup>* and *Irf3<sup>Δ/Δ</sup>* mouse lungs was analyzed for *Tnf* and *Il1b* by qRT-PCR. The results are representatives of at least two to three independent experiments. The data represent means  $\pm$  SEM;  $n = 2$  to 4, where applicable, each dot represents one mouse and is an average of the three technical replicates. \* $P < 0.05$ , \*\* $P < 0.005$ , \*\*\* $P < 0.0005$ , and \*\*\*\* $P < 0.0001$ .

*Cd8* mRNA levels, however, did not significantly change in *Irf3*<sup>Δ/Δ</sup> mice (fig. S3, A and B). Similar increase in macrophage markers (*Cd68* and *F4/80*) was also observed in MHV-infected *Irf3*<sup>Δ/Δ</sup> lungs (Fig. 3, I and J). To specifically examine whether increased macrophages contributed to elevated inflammatory genes in *Irf3*<sup>Δ/Δ</sup> mice, we performed enrichment analyses by isolating macrophage population from lung single-cell suspension from SeV-infected mice. Enrichment analyses, as expected, showed increased macrophage marker (*F4/80*) in *Irf3*<sup>Δ/Δ</sup> lungs (Fig. 3K). The purity of the enriched pool was ensured by the absence of *Cd4* (T cell marker) or *Ly6g* (neutrophil marker) expression (Fig. 3K). Enriched *Irf3*<sup>Δ/Δ</sup> macrophage population showed increased *Tnf* and *Il1b* levels (Fig. 3, L and M). Overall, IRF3 prevented respiratory viral pathogenesis by inhibiting macrophage infiltration to infected lungs.

### Macrophage-specific IRF3 prevents lung inflammation and viral pathogenesis

Increased lung inflammation, in combination with increased infiltrating macrophages, led us to examine macrophage-specific role of IRF3 in viral pathogenesis. The heterozygotes (*Irf3*<sup>fl/fl</sup>), which were sufficient to protect against SeV infection (Fig. 1, F and G), were crossed with macrophage-specific Cre deleter mice (*Cre*<sup>LysM</sup>) to generate mice

with the deletion of *Irf3* in macrophages (*Irf3*<sup>MKO</sup>; Fig. 4A). The deletion of IRF3 protein was confirmed by immunoblot analyses in isolated primary BMDMs from *Irf3*<sup>MKO</sup> mice (Fig. 4B). Lung viral load was enhanced in *Irf3*<sup>MKO</sup> mice compared to the control (*Irf3*<sup>fl/fl</sup>) mice (Fig. 4C). *Tnfaip3*-encoded A20 protein levels were higher in *Irf3*<sup>MKO</sup> mouse lungs, indicating increased NF-κB-dependent gene expression (Fig. 4D). Cytokine expression—measured by quantitative reverse transcription polymerase chain reaction (qRT-PCR) of *Il1b*, *Il1a*, *Tnfaip3*, and *Tnf* genes—was enhanced in *Irf3*<sup>MKO</sup> lungs (Fig. 4, E to H), suggesting that IRF3 in macrophages was primarily responsible for the anti-inflammatory function of IRF3 during SeV infection. Increased inflammatory genes, as expected, were accompanied by increased macrophage accumulation in infected lungs of *Irf3*<sup>MKO</sup> (Fig. 4, I to K). Immunofluorescence staining of the SeV-infected lung sections indicated increased levels of *F4/80* (Fig. 4, L and M, and fig. S4A), a pan macrophage marker, and *CD68* (Fig. 4, N and O, and fig. S4B), an inflammatory macrophage marker, in *Irf3*<sup>MKO</sup> mice. Furthermore, *Irf3*<sup>MKO</sup> mice showed unaltered T cell levels, analyzed by *CD3e* immunostaining (fig. S4, C and D); neutrophils, analyzed by *Ly6G* immunostaining (fig. S4, E and F); and dendritic cells, analyzed by *CD11c* immunostaining (fig. S4, G and H). Increased inflammatory

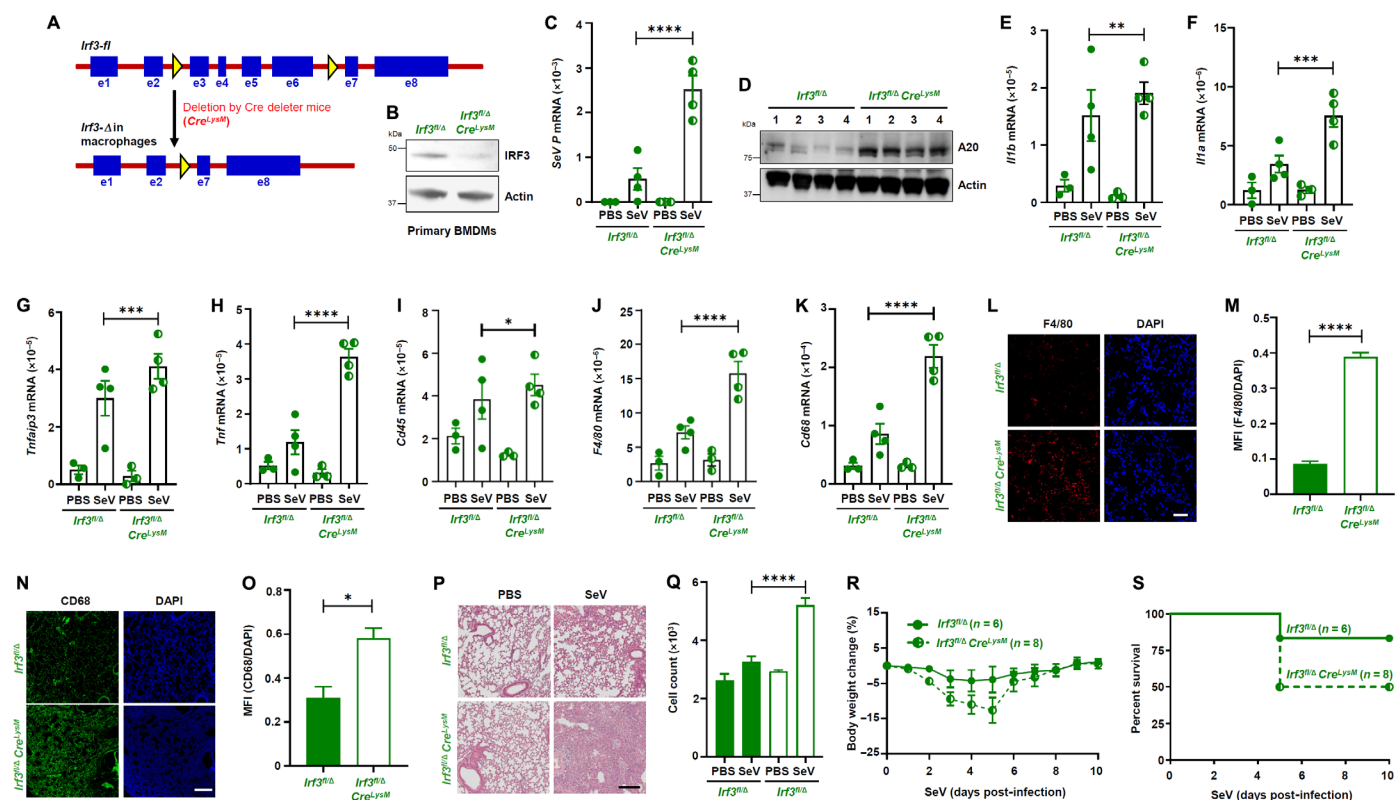


**Fig. 4. *Irf3* deficiency in macrophages leads to increased lung inflammation and viral pathogenesis.** (A) A schematic showing the generation of *Irf3*<sup>MKO</sup> mice (*Irf3*<sup>fl/fl</sup> *Cre*<sup>LysM</sup>) by crossing *Irf3*<sup>fl/fl</sup> mice with LysM-driven Cre-expressing mice (*Cre*<sup>LysM</sup>). (B) Primary BMDMs from *Irf3*<sup>fl/fl</sup> and *Irf3*<sup>fl/fl</sup> *Cre*<sup>LysM</sup> mice were used to analyze IRF3 expression by immunoblot. (C to S) *Irf3*<sup>fl/fl</sup> and *Irf3*<sup>fl/fl</sup> *Cre*<sup>LysM</sup> mice were intranasally infected with SeV (425,000 PFU per mouse), and the following analyses were performed: lung viral mRNA expression by qRT-PCR (C), A20 expression in lung homogenates by immunoblot (D), mRNA levels of inflammatory markers (*Il1b*, *Il1a*, *Tnfaip3*, and *Tnf*) and macrophage markers (*Cd45*, *F4/80*, and *Cd68*) by qRT-PCR [(E) to (K)], *F4/80* immunostaining and quantification on infected lung sections [(L) and (M)], *CD68* immunostaining and quantification on infected lung sections [(N) and (O)], lung histology by H&E staining (P), quantification of multiple H&E stained sections from two different mice (Q), body weight changes (R), and survival (S) of the infected mice. The results are representatives of at least two to three independent experiments. The data represent means  $\pm$  SEM;  $n = 2$  to 4, where applicable, each dot represents one mouse and is an average of the three technical replicates. \* $P < 0.05$ , \*\* $P < 0.005$ , \*\*\* $P < 0.0005$ , and \*\*\*\* $P < 0.0001$ . Scale bars, 50  $\mu$ m (L) and 200  $\mu$ m [(N) and (P)]. MFI, mean fluorescence intensity.

cytokines and infiltrated macrophage population resulted in lung immunopathology in *Irf3*<sup>MKO</sup> mice (Fig. 4, P and Q, and fig. S4I). Together, the increased inflammatory responses led to enhanced viral pathogenesis in *Irf3*<sup>MKO</sup> mice, evidenced by increased body weight loss (Fig. 4R) and mortality (Fig. 4S). Overall, IRF3 in macrophages was critical to prevent SeV-induced lethality.

### IRF3 in macrophages contributes to its anti-inflammatory but not transcriptional or pro-apoptotic functions in SeV-infected lungs

Because IRF3 in macrophages was critical to prevent SeV-induced viral inflammation and pathogenesis, we inquired whether other functions of IRF3 were affected by the deletion of *Irf3* in these cells. To address this, we performed RNA sequencing (RNA-seq) analyses of the total lung from mock-infected or SeV-infected control (*Irf3*<sup>f/f</sup>)

and *Irf3*<sup>MKO</sup> mice using three mice from each group. Heatmap analyses revealed that 12,710 genes were significantly differentially expressed between mock-infected and SeV-infected control (*Irf3*<sup>f/f</sup>) and *Irf3*<sup>MKO</sup> mice (Fig. 5A). We focused on differential gene expression patterns between SeV-infected control and *Irf3*<sup>MKO</sup> mice. Venn diagram showed both overlapping and differentially expressed genes between these groups (Fig. 5B). Kyoto Encyclopedia of Genes and Genomes (KEGG) pathway analyses revealed that genes involved in inflammatory signaling pathways were significantly up-regulated in these mice (Fig. 5C). We focused on NF-κB signaling pathway, which is critical for inflammatory gene expression. Targeted analyses of NF-κB signaling pathway and a select subset of NF-κB-dependent genes further revealed their up-regulation in *Irf3*<sup>MKO</sup> mice (Fig. 5D). Next, we evaluated IFN and ISG expression from RNA-seq analyses. SeV infection, as expected, enhanced many IFN and ISGs compared

Downloaded from https://www.science.org on April 11, 2025

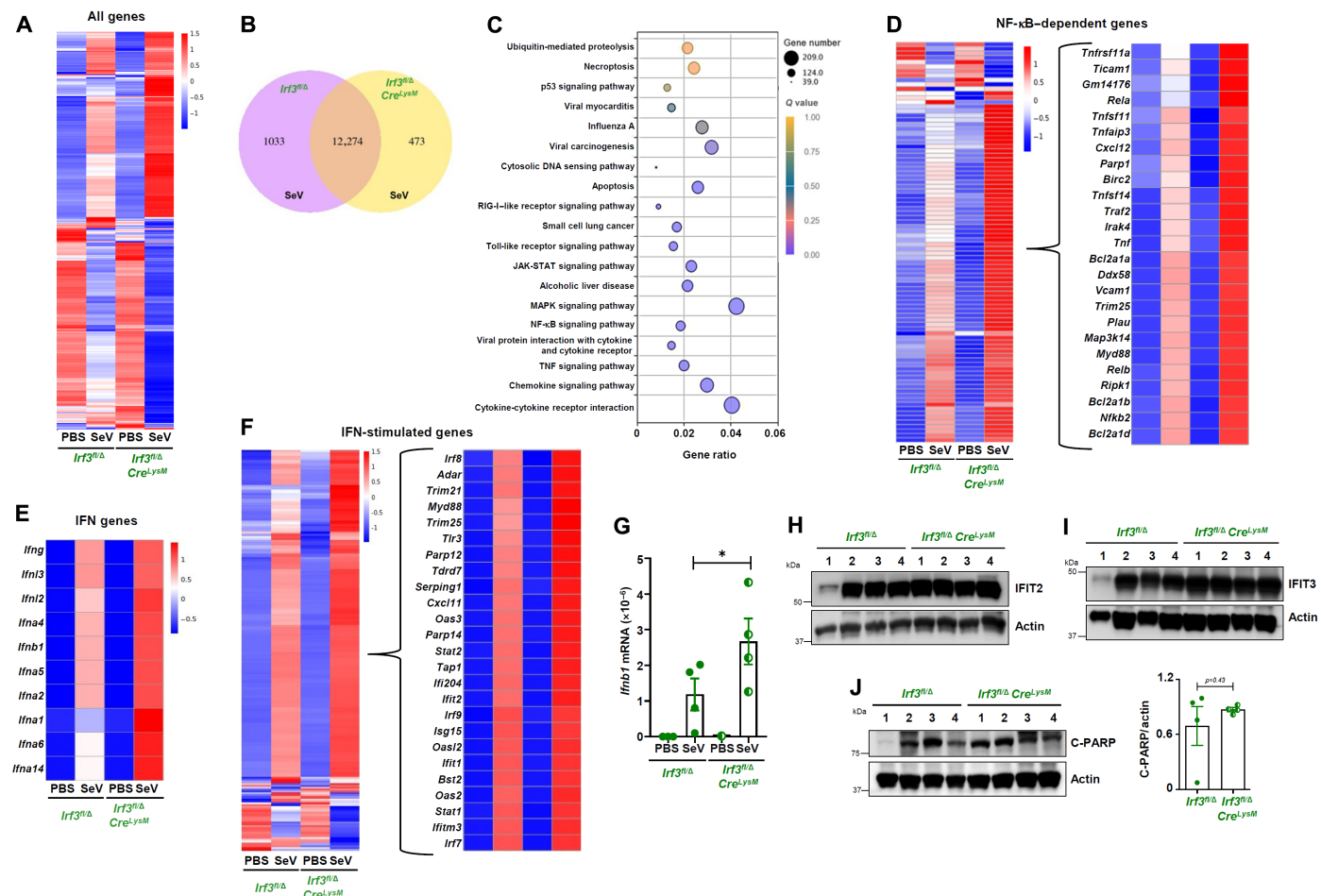


**Fig. 5. RNA-seq analyses revealed *Irf3* deficiency in macrophages leads to increased NF-κB-induced genes, with no defects in IFN and pro-apoptotic responses in virus-infected lungs.** (A) Heatmap showing differentially expressed 12,710 genes in mock-infected or SeV-infected lungs from *Irf3*<sup>f/f</sup> and *Irf3*<sup>f/f</sup> *Cre*<sup>LysM</sup> mice (P value ≤ 0.05, |log2(fold change)| ≥ 0.0). (B) Venn diagram showing the number of differentially expressed and overlapping genes in infected *Irf3*<sup>f/f</sup> and *Irf3*<sup>f/f</sup> *Cre*<sup>LysM</sup> mice. (C) KEGG analyses of selected differentially regulated pathways in *Irf3*<sup>f/f</sup> and *Irf3*<sup>f/f</sup> *Cre*<sup>LysM</sup> mice. (D) Heatmap showing 90 NF-κB-dependent genes, identified by KEGG analyses (left), and a subset of 25 selected examples (right). (E) Heatmap showing IFN genes, differentially regulated in *Irf3*<sup>f/f</sup> and *Irf3*<sup>f/f</sup> *Cre*<sup>LysM</sup> mice. (F) Heatmap showing 214 ISGs, differentially expressed, in *Irf3*<sup>f/f</sup> and *Irf3*<sup>f/f</sup> *Cre*<sup>LysM</sup> mice and a subset of 25 selected examples (right). (G) *Ifnb1* mRNA levels were analyzed by qRT-PCR in *Irf3*<sup>f/f</sup> and *Irf3*<sup>f/f</sup> *Cre*<sup>LysM</sup> mouse lungs. (H and I) Lung homogenates from *Irf3*<sup>f/f</sup> and *Irf3*<sup>f/f</sup> *Cre*<sup>LysM</sup> mice were analyzed for IFIT2 and IFIT3 protein expression by immunoblot. (J) Lung homogenates from *Irf3*<sup>f/f</sup> and *Irf3*<sup>f/f</sup> *Cre*<sup>LysM</sup> mice were analyzed for cleaved poly(adenosine 5'-diphosphate-ribose) polymerase (C-PARP) levels by immunoblot and quantified by ImageJ. The results are an average of three mice from each group. The data represent means ± SEM; n = 2 to 4, where applicable, each dot represents one mouse and is an average of the three technical replicates. \*P < 0.05.

to mock-infected control mice. The deletion of *Irf3* in macrophages did not have any defects in the overall expression levels of IFNs and ISGs (Fig. 5, E and F). We validated the RNA-seq results using qRT-PCR analyses, and *Irf3<sup>MKO</sup>* mice did not display defective *Ifnb1* expression in SeV-infected lungs (Fig. 5G). We further evaluated specific antiviral ISGs, IFIT2 and IFIT3 expression, by immunoblot of lung homogenates; their protein levels were largely unaltered in *Irf3<sup>MKO</sup>* mice (Fig. 5, H and I). IRF3 is involved in apoptotic killing of virus-infected cells by RIPA (22). Levels of cleaved poly(adenosine 5'-diphosphate-ribose) polymerase (C-PARP), an apoptotic cell death marker, however, were comparable between control and *Irf3<sup>MKO</sup>* mice (Fig. 5J). These results indicated that *Irf3* deletion in macrophages, although augmented the lung inflammatory responses, did not however cause defective transcriptional or pro-apoptotic responses in the infected lungs.

### Macrophage-specific IRF3 inhibits pro-inflammatory and enhances anti-inflammatory, macrophage infiltration to the site of infection

Macrophages differentiate into two phenotypically distinct subpopulations depending on their milieu. The classically activated or M1 macrophages are pro-inflammatory, and the alternatively activated or the M2 macrophages are anti-inflammatory (36, 37). To investigate the phenotype of the macrophages in the SeV-infected lungs, we performed targeted analyses of the RNA-seq results for markers of M1 and M2 macrophages, which regulate inflammatory responses during virus infection. *Irf3<sup>MKO</sup>* mice, as expected, displayed enhanced expression of *Cd68* and *F4/80*, markers of macrophages (Fig. 6A). Furthermore, *Nos2*, *Cd86*, and *Cd80*, markers of M1 macrophages, were increased, and *Fizz*, *Cd200*, and *Cd163*, markers of M2 macrophages, were reduced in *Irf3<sup>MKO</sup>* mice compared to control mice (Fig. 6A). RNA-seq results were first validated in *Irf3<sup>Δ/Δ</sup>* mice, which, compared to control mice (*Irf3<sup>fl/fl</sup>*), expressed higher levels of *Nos2* and *Cd80* in SeV-infected lungs (Fig. 6, B and C). Subsequently, *Fizz* levels were reduced in SeV-infected *Irf3<sup>Δ/Δ</sup>* lungs (Fig. 6D). We further compared these macrophage markers between *Irf3<sup>MKO</sup>* and *Irf3<sup>fl/Δ</sup>* mice. *Irf3<sup>MKO</sup>* mice showed increased *Nos2* and *Cd80* and reduced *Fizz* levels in SeV-infected lungs (Fig. 6, E to G). The qRT-PCR results were further confirmed using flow cytometry; CD80-expressing cells were increased (Fig. 6H and fig. S5A), whereas CD163-expressing cells were reduced (Fig. 6I and fig. S5B) in *Irf3<sup>MKO</sup>* lungs upon SeV infection. Immunofluorescence in lung sections of SeV-infected *Irf3<sup>fl/Δ</sup>* and *Irf3<sup>MKO</sup>* mice confirmed higher levels of CD80 (Fig. 6, J and K, and fig. S5C) and reduced CD163 expression (Fig. 6, L and M, and fig. S5D) in the *Irf3<sup>MKO</sup>* mice. Together, our results indicated macrophage-specific IRF3 inhibited infiltration of pro-inflammatory macrophages and augmented anti-inflammatory macrophages to SeV-infected lungs.

### Macrophage IRF3 inhibits inflammatory and stress signaling pathways in SeV-infected lungs

Pathological responses during virus infection are regulated by cumulative action of inflammatory (e.g., NF-κB) and stress [e.g., mitogen-activated protein kinase (MAPK)] signaling pathways (38–43). To specifically evaluate whether IRF3 in macrophages inhibits, in addition to NF-κB signaling, other stress responses, we performed immunoblot analyses of MAPK signaling activation. *Irf3<sup>MKO</sup>* lung homogenates displayed significantly increased levels of phospho-p38 MAPK (p-p38; Fig. 7A), phospho-c-Jun N-terminal kinase (p-JNK)

(Fig. 7B), and phospho-extracellular signal-regulated kinase (p-ERK) (Fig. 7C), which are major regulators of cellular stress responses. As expected, *Irf3<sup>MKO</sup>* mice showed increased p-p65, a signature of canonical NF-κB activation, in SeV-infected lungs (Fig. 7, D to F, and fig. S6A). p-p65 levels were enhanced in *Irf3<sup>MKO</sup>* lung macrophages, analyzed by co-immunostaining of p-p65 and F4/80, compared to the control mice (Fig 7G and fig. S6B). These results indicated that IRF3 was responsible for suppressing NF-κB activation (p-p65) in macrophages during SeV infection. Last, we evaluated whether these pathways were also up-regulated in *Irf3<sup>Δ/Δ</sup>* mice. SeV-infected lung sections and homogenates from *Irf3<sup>Δ/Δ</sup>* mice showed increased p-p65 levels, analyzed by immunofluorescence staining (Fig. 7, H and I, and fig. S6C), and p-p38 levels, analyzed by immunoblot (Fig. 7J), respectively, compared to control (*Irf3<sup>fl/fl</sup>*) mice. Together, the pathogenic effects of *Irf3* deficiency in macrophages were mediated by enhanced inflammatory and stress signaling pathways in SeV-infected lungs.

### DISCUSSION

In this study, we identified the cell type in which IRF3 is required for suppressing inflammatory responses and, subsequently, viral pathogenesis (Fig. 7K). Virus infection activates IRF3 as a transcription factor by phosphorylation, which leads to its nuclear translocation and induction of antiviral genes (17, 36, 44–46). In addition to its nuclear function, we uncovered that virus-induced ubiquitination of IRF3 causes its mitochondrial translocation, resulting in activation of pro-apoptotic cell death (22, 47, 48). Recently, we demonstrated that IRF3 also functions as an anti-inflammatory protein, independent of its transcriptional or pro-apoptotic activities, during virus infection (25, 26). For anti-inflammatory function, IRF3 interacts directly with NF-κB–p65 subunit, sequestering it in the cytosol, thereby preventing nuclear translocation. *Irf3* deficiency leads to increased NF-κB-dependent inflammatory gene expression in virus-infected cells and mice. Although the molecular mechanism of IRF3-mediated NF-κB inhibition was identified, the physiological relevance of this function remained unclear. Here, we used conditional *Irf3* knockout (*Irf3<sup>Δ/Δ</sup>*) and macrophage-specific *Irf3* knockout (*Irf3<sup>MKO</sup>*) mice to evaluate the role of IRF3 in preventing viral inflammation and pathogenesis. *Irf3<sup>Δ/Δ</sup>* mice, upon respiratory viral infection, exhibited increased inflammatory gene expression, lung damage, and mortality. Susceptibility of *Irf3<sup>Δ/Δ</sup>* mice was accompanied by increased macrophage abundance in the infected lungs. Macrophage-specific *Irf3* deletion, similar to the deletion of *Irf3* from all cell types (*Irf3<sup>Δ/Δ</sup>*), augmented lung inflammation and mortality, demonstrating that IRF3 in macrophages was required for suppressing viral inflammation. RNA-seq analyses revealed increased inflammatory and MAPK signaling activation in infected *Irf3<sup>MKO</sup>* mice. We, therefore, postulate that IRF3 in macrophages is critical to suppress lung inflammatory responses and, subsequently, prevent viral pathogenesis.

A major finding from our study was that the lack of IRF3 in macrophages did not cause defective transcriptional or pro-apoptotic functions in infected lungs. These functions of IRF3 were not sufficient to prevent viral pathogenesis, suggesting the critical anti-inflammatory role of IRF3. We further revealed, by RNA-seq and qRT-PCR analyses, increased expression of IFNs in *Irf3<sup>MKO</sup>* mice. Because IFNs contribute to host inflammatory responses, future studies will reveal whether overproduction of IFNs is pathologic in

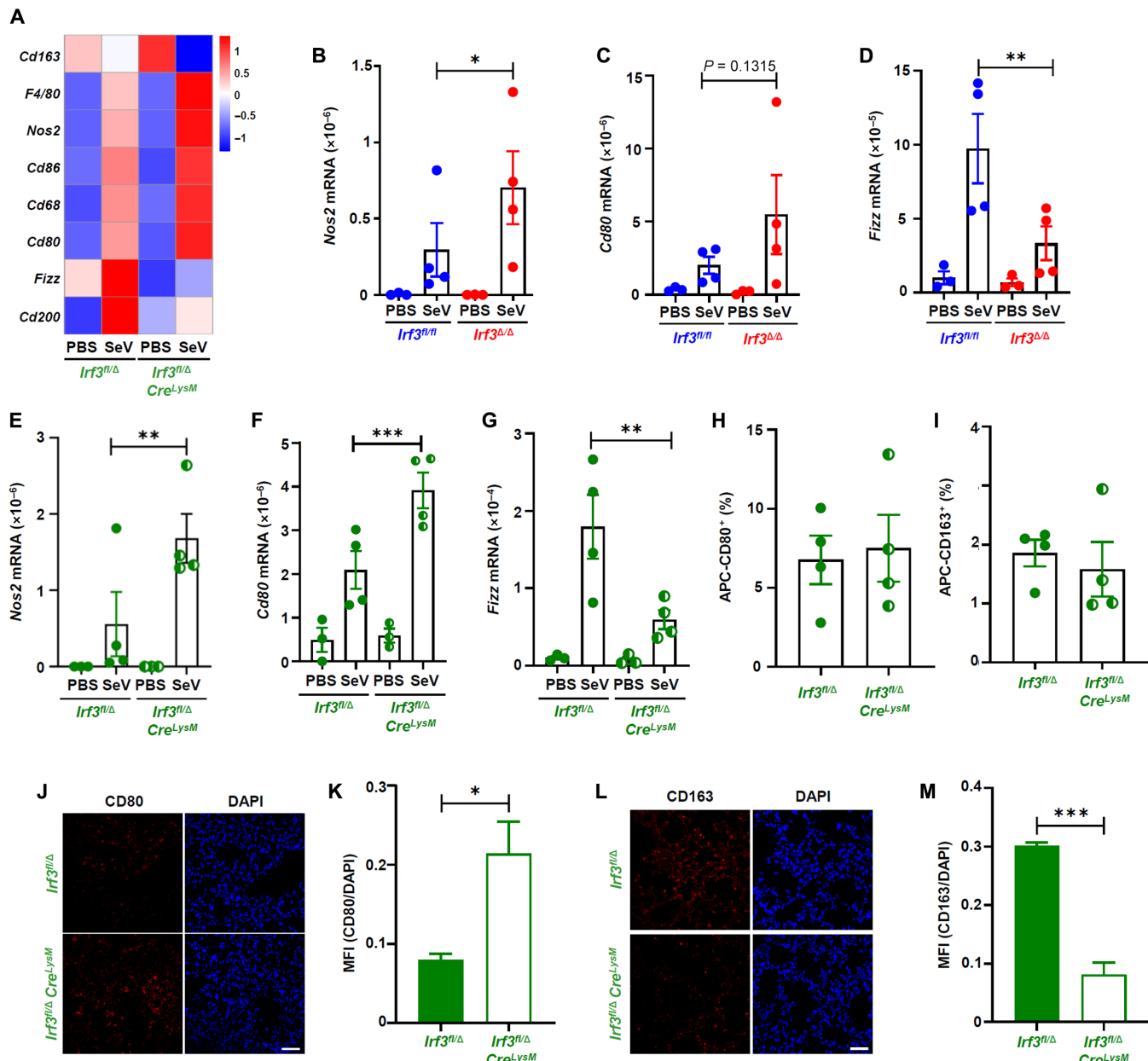


**Fig. 6.** *Irf3* deficiency causes increased pro-inflammatory macrophages and decreased anti-inflammatory macrophages in virus-infected lungs. (A) Heatmap, derived from RNA-seq analyses, showing levels of macrophage markers in mock-infected or SeV-infected lungs from *Irf3<sup>fl/fl</sup>* and *Irf3<sup>Δ/Δ</sup> Cre<sup>LysM</sup>* mice. (B to D) qRT-PCR analyses of macrophage markers (*Nos2*, *Cd80*, and *Fizz*) in SeV-infected lungs from *Irf3<sup>fl/fl</sup>* and *Irf3<sup>Δ/Δ</sup>* mice, 7 days postinfection. (E to G) qRT-PCR analyses of macrophage markers (*Nos2*, *Cd80*, and *Fizz*) in SeV-infected lungs from *Irf3<sup>fl/fl</sup>* and *Irf3<sup>fl/fl</sup> Cre<sup>LysM</sup>* mice. (H and I) Flow cytometric analyses of *CD80* and *CD163* expression in single-cell suspension of SeV-infected lungs of *Irf3<sup>fl/fl</sup>* and *Irf3<sup>fl/fl</sup> Cre<sup>LysM</sup>* mice. (J and K) *CD80* immunostaining and quantification on SeV-infected lung sections. (L and M) *CD163* immunostaining and quantification on SeV-infected lung sections. The results are an average of three mice from each group. The data represent means  $\pm$  SEM;  $n = 2$  to 4, where applicable, each dot represents one mouse and is an average of the three technical replicates. \* $P < 0.05$ , \*\* $P < 0.005$ , \*\*\* $P < 0.0005$ . Scale bars, 50  $\mu\text{m}$  [(J) and (L)]. DAPI, 4',6-diamidino-2-phenylindole.

*Irf3<sup>MKO</sup>* mice. In our previous studies, we showed a protective role of IRF3 by its nontranscriptional mutant (Irf3-S1) is unaffected in *Irf3<sup>S1/S1</sup> Ifnar1<sup>-/-</sup>* mice, suggesting that type I IFNs had no major impact in Irf3-mediated protection against SeV infection (22). In contrast, *Irf2<sup>-/-</sup>* mice, which are highly susceptible to SeV infection, are protected when crossed with *Ifnar1<sup>-/-</sup>* mice, suggesting a pathologic role of IFN in SeV-induced pathogenesis (49). In the future, *Irf3<sup>MKO</sup>* mice will be crossed with *Ifnar1<sup>-/-</sup>* mice to evaluate the role

of IFNs. IRF3-induced IFN- $\beta$  contributes to lipopolysaccharide (LPS)-mediated septic shock (50, 51); *Irf3<sup>-/-</sup>* mice are resistant due to reduced IFN- $\beta$  upon LPS treatment (51). In this context, a critical role of IRF3 in macrophages was revealed (50); *Irf3<sup>MKO</sup>* mice, similar to *Irf3<sup>-/-</sup>* mice, were protected from LPS-induced toxicity. Unexpectedly, *Irf3* deletion in dendritic cells, although inhibits IFN- $\beta$  levels, does not protect mice from LPS-mediated septic shock (50). These results indicate that macrophagic IRF3-induced IFN- $\beta$

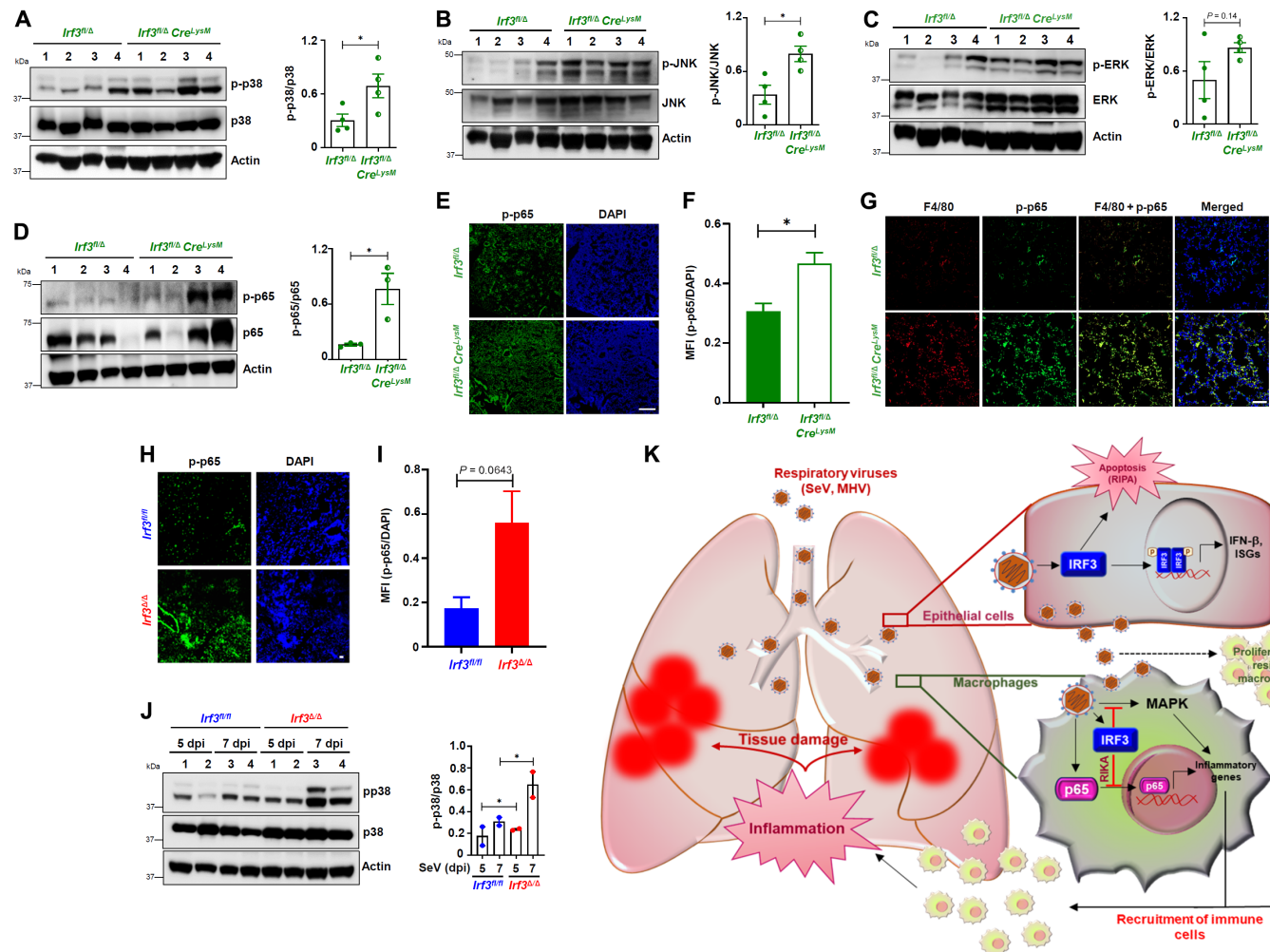


**Fig. 7. *Irf3* deficiency in macrophages leads to increased MAPK and NF-κB signaling in infected mouse lungs.** (A to G) *Irf3<sup>fl/fl</sup>* and *Irf3<sup>fl/fl</sup> Cre<sup>LysM</sup>* mice were intranasally infected with SeV (425,000 PFU per mouse), and the following analyses were performed: The lung homogenates were analyzed for p-p38 MAPK (A), p-JNK (B), p-ERK (C), and p-p65 (D) by immunoblot and quantified by ImageJ. Lung sections were immunostained for p-p65 and quantified [(E) and (F)] or co-immunostained for F4/80 and p-p65 (G). (H to J) *Irf3<sup>fl/fl</sup>* and *Irf3<sup>Δ/Δ</sup>* mice were intranasally infected with SeV (425,000 PFU per mouse); lung sections were analyzed for p-p65 by immunofluorescence and quantified [(H) and (I)], and lung homogenates were analyzed for p-p38 MAPK by immunoblot and quantified using ImageJ (J). (K) A model showing putative cell type-specific roles of different functions of IRF3 leading to protection against viral pathogenesis. The results are representatives of at least two to three independent experiments. The data represent means ± SEM;  $n = 2$  to 4, where applicable, each dot represents one mouse and is an average of the three technical replicates. \* $P < 0.05$ . Scale bars, 200 μm (E), 50 μm (G), and 20 μm (H).

contributes to LPS-induced sepsis. Pathologic and inflammatory effects of IFN-β have been shown in SARS-CoV-2 infection; uncontrolled IFN signaling contributes to SARS-CoV-2 inflammation and pathogenesis in rhesus monkeys (52). We revealed that IRF3, although critical for *Ifnb1* induction in primary BMDMs (Fig. 3, B and E), its absence in macrophages did not affect *Ifnb1* synthesis in infected tissue (Fig. 5G) (53). These results suggest pathologic effects of IFN-β, if any, might be induced by nonmacrophagic IRF3. Pro-apoptotic function of IRF3 is speculated to eliminate virus-infected cells from the tissue and contribute to antiviral responses. *Irf3<sup>MKO</sup>* mice were not defective in pro-apoptotic function of IRF3 in infected lungs; however, this function was not sufficient to prevent viral pathogenesis. These results, together, highlighted the critical role of IRF3 in attenuating lung inflammation, a major cause of respiratory viral pathogenesis. Whether lack of RIPA-mediated

cell death in *Irf3<sup>-/-</sup>* cells contributes to increased inflammation was evaluated by blocking apoptosis using a pan-caspase inhibitor. Apoptotic inhibitor, indeed, led to increased inflammatory gene expression and, as expected, viral load in immortalized BMDMs (iBMDMs) (fig. S7). Inhibition of apoptosis is a physiologically relevant scenario in many viral infections because viruses often express proteins to block apoptotic cell death. Viruses can achieve multiple goals by blocking cell death—keeping the cells alive to facilitate productive life cycle and increasing inflammation, as also observed in our results, to cause organ damage. These results indicate a cross-talk between RIPA and RIKA in regulating viral pathogenesis; however, extensive validation of these results will require mice defective in specific IRF3 pathways.

Optimal antiviral response of IRF3 is a cumulative effect of its activities in multiple cell types. We postulate that macrophage-specific

IRF3 is responsible for its anti-inflammatory function in the infected tissue. We speculate that other cell types, e.g., AECs, may be the early and primary responders of protective transcriptional and pro-apoptotic functions of IRF3 (Fig. 7K). Intranasal virus exposure infects AECs in early phase when virus replicates rapidly for spreading to other cells and organs. IRF3 is activated during early phase and likely contributes to antiviral gene expression by its transcriptional pathway. These cells may also support pro-apoptotic function of IRF3, which requires virus-induced activation. Using antibodies to probe phosphorylated (for transcriptional branch) or ubiquitinated (for pro-apoptotic branch) IRF3 in conjugation with AEC marker can help clarify these points. In the future, AEC-specific deletion of *Irf3* may help elucidate this genetically. Our results indicated that IRF3 in macrophages was critical for preventing inflammatory responses. Moreover, an increase in the F4/80 expression, a marker of tissue resident macrophages, was observed in the infected lungs of both our deletion models (global and macrophage specific). In situ proliferation of macrophages for immune defense and self-renewal play a major role in driving inflammatory responses (54). Besides AECs, the proliferation of resident macrophages contributes to increased inflammatory response and recruitment of immune cells, such as neutrophils, macrophages, dendritic cells, etc., to the site of infection. *LysM* is expressed, although primarily in macrophages, also in neutrophils, and monocytes (55–57). In the future, we will investigate whether these cells also play any protective roles against virus infection. Because neutrophils are early responders to the infection site, whether their infiltration is also regulated by IRF3 will be investigated. Dendritic cells, which primarily induce TLR-dependent immune responses, will be investigated using cell-specific Cre deleters. *Cre<sup>LysM</sup>*-mediated deletion of *Irf3*, although partially phenocopied *Irf3<sup>Δ/Δ</sup>* mice during SeV infection, had no impact on encephalomyocarditis virus (EMCV)-mediated pathogenesis (50). These results suggest that EMCV pathogenesis is controlled by IRF3 in nonmyeloid cells.

Another major finding from our studies is that macrophage-specific IRF3 controls, in addition to NF-κB signaling, MAPK signaling pathways. *Irf3<sup>MKO</sup>* mice showed increased p-p38, p-JNK, and p-ERK, which control inflammatory and stress responses of the host. How IRF3 regulates MAPK signaling pathways in macrophages will require in-depth investigation. Whether IRF3 physically interacts with some or any common signaling molecule in these pathways will be a central theme of future studies. MAPK signaling controls host inflammatory responses directly or by regulating inflammatory pathways, e.g., NF-κB and IFN signaling. The p38 MAPK pathway also regulates inflammasome activation (40, 42); whether the observed hyperinflammation in *Irf3* deficiency is due to inflammasome activation will require further investigation. Human microglial cells confer anti-inflammatory response by adenovirus-mediated expression of IRF3 (58). Ad-IRF3 activates phosphatidylinositol 3-kinase (PI3K)/AKT signaling pathway to suppress inflammatory responses of glial cells. In-depth investigation will be required to conclude whether PI3K/AKT signaling pathway also regulates the inflammatory responses observed in *Irf3<sup>MKO</sup>* mice. Because viruses take advantage of these pathways to facilitate replication and spread, host-centric studies need to be complemented by studying viral proteins that suppress antiviral responses. Viral proteins may specifically inhibit one function of IRF3, without affecting others, to take control of the host. Engineered viruses that replicate efficiently may be effective tools for these studies.

Our study revealed the role of NF-κB and MAPK signaling pathways in viral pathogenesis and IRF3 inhibits them to prevent this.

Targeting these signaling pathways in mice may be an effective strategy to prevent respiratory viral disease. Some of these inhibitors have been tested in various virus infection studies and showed potential in treating viral diseases (59, 60). Because many viruses block IRF3 to facilitate their replication, strategies should be made to test these inhibitors in viral pathogenesis studies. Besides the inhibitors, cell-permeable IRF3-derived peptides can be designed using knowledge gained from IRF3–NF-κB domain mapping studies (26). These peptides would specifically block NF-κB functions without affecting IRF3 activities and open up avenues for future clinical applications of our study. Moreover, lung macrophage–targeted drug delivery through liposomes or nanoparticles is a promising therapeutic approach to ameliorate lung fibrosis and respiratory distress syndrome (61, 62). It will need further in-depth studies to uncover an effective drug-delivery approach for lung macrophages, without affecting inflammatory response from other cells in the milieu or triggering adverse immunogenicity from the host. In addition to viruses, many bacterial infections lead to severe inflammatory pathogenesis. Future work would be required to examine whether RIKA has any protective role in these contexts, particularly where IRF3 has antimicrobial functions (63). IRF3 has been studied, in addition to microbial infections, in liver diseases and cancer (64, 65). In these scenarios, specific IRF3-dependent pathways can be evaluated when mice expressing pathway-specific IRF3 mutants are generated. Overall, our study takes us a step closer to a targeted therapeutic approach, such that the host still retains adequate inflammatory responses indispensable for fighting the virus infection but can also suppress undesired outcomes of hyperinflammation.

## MATERIALS AND METHODS

### **Mice, primary cells, viruses, and virus infection**

*Irf3* *fl* (*Irf3<sup>fl/fl</sup>*) and *delta* (*Irf3<sup>Δ/Δ</sup>*) mice were generated in C57BL/6 background. *Irf3<sup>MKO</sup>* mice were generated by crossing *Irf3<sup>fl/Δ</sup>* mice with *Cre<sup>LysM</sup>* mice from the Jackson Laboratories (#004781). SeV Cantell and 52 strains were obtained from Charles River Laboratories. MHV-A59 was obtained from BEI and propagated in the laboratory using previously described procedures (26, 66). The study involved both male and female mice, between 8 and 12 weeks of age. SeV infections in mice were performed using two different doses [125,000 and 425,000 plaque-forming units (PFU)] of SeV 52 strain, administered intranasally. For MHV infection, each mouse was infected with 10<sup>6</sup> PFU of virus intranasally. Intranasal virus inoculation was performed after isoflurane-induced anesthesia, and the infected mice were weighed once daily to monitor the body weight loss. The mice were euthanized when body weight dropped to 80% of their initial weight. Primary BMDMs were isolated from the *Irf3<sup>fl/fl</sup>* and *Irf3<sup>Δ/Δ</sup>* male and female mice following previously described procedure (22). All animal procedures are approved by the University of Toledo Institutional Animal Care Committee under protocol 108668. MEFs were obtained from the mice and immortalized by continuous passaging, as described before (22). MEFs were cultured in Dulbecco's Modified Eagle Medium (DMEM) containing 10% fetal bovine serum (FBS) and antibiotics. iBMDMs, obtained from BEI, described previously (26, 27), were cultured in DMEM containing 10% FBS and antibiotics.

### **Genotyping of the mice**

DNA was isolated from ear punches of the mice using sodium hydroxide extraction, and multiplex PCR was performed using this

DNA. The PCR products were run on a 2.5% agarose gel to image the amplification products. The primers used were as follows: Irf3\_fwd: ACTCTGGAAATGAGTAAGGGTTTCTGC, Irf3\_rev1: CA-CAGGTCTTCCTCACCATTTGTGTAC, Irf3\_rev2: GCCACATTC TTCAAAGGCTGC, Cre\_fwd: GAACGCACTGATTTCGACCA, and Cre\_rev: GCTAACCGAGCGTTTCGTT.

### Immunoblotting

For immunoblot analyses, small portions of mouse lungs were homogenized using a mechanical homogenizer in a 50 mM tris buffer (pH 7.4) containing 150 mM NaCl, 0.1% Triton X-100, 1 mM sodium orthovanadate, 10 mM sodium fluoride, 10 mM  $\beta$ -glycerophosphate, 5 mM sodium pyrophosphate, and protease inhibitors (Roche) on ice. These were then further vortexed and centrifuged to separate out the clear lysate. Bradford assay was performed for protein quantification in these lysates using Bradford reagent (Bio-Rad, #500-0006). Equal amounts of total protein were used to perform SDS-polyacrylamide gel electrophoresis followed by which blots were probed with antibodies against various proteins of interest. Actin was used as the loading control. The following antibodies were used to probe the specific proteins shown in the figures: IL-1 $\beta$  [Cell Signaling Technology (CST), #12242], A20 (CST, #5630S), C-PARP (CST, #9548S), IFIT2 and IFIT3 [as described before (23)], IRF3 (Novus Biologicals, #NBP1-78769), NF- $\kappa$ B p-p65 (CST, #3033S), NF- $\kappa$ B p65 (CST, #8242S), p-p38 (CST, #4511S), p38 (CST, #9212S), p-JNK (CST, #9251), JNK (CST, #9252), p-ERK (CST, #4370S), ERK (CST, #4695S), IRF7 (CST, #39659S), glyceraldehyde-3-phosphate dehydrogenase (CST, #5174S), and actin (Sigma-Aldrich, #5441).

### Quantitative RT-PCR

RNAs from small portions of mouse lungs, either mock-infected or infected with SeV or MHV, as indicated in figures, were extracted using TRIzol (Sigma-Aldrich, #1003553429). This pool of total RNA was deoxyribonuclease (DNase)-treated (Promega) and then used to perform RT-PCR to generate the cDNA pool using the Im-Prom II reverse transcription kit from Promega. The cDNA was subjected to amplification of genes of interest using specific primers. Amplification was quantified using Radian SYBR Green PCR mix (Alkali Scientific Inc.) in Roche LightCycler 96 instrument. Data were analyzed using LightCycler 480 Software version 1.5. The expression levels of the different genes analyzed were normalized to the 18S ribosomal RNA expression level, and data were plotted using GraphPad Prism 9 software. The primers for genes analyzed are listed in table S1.

### Bulk RNA-seq and analysis

RNA was isolated from the lungs of SeV-infected *Irf3*<sup>fl/fl</sup> and *Irf3*<sup>MKO</sup> mice using the TRIzol method. The isolated RNA was further cleaned up using an RNeasy plus mini kit (QIAGEN, #74136). The quality and quantity of isolated RNA were then confirmed using NanoDrop 2000 and sent to Novogene for RNA-seq. After quality control tests, mRNA library was constructed using polyadenylate tail capture via oligo(dT) beads and again tested for quality control. The library generated was sequenced using Illumina platform (NovaSeq 6000) with pair-end 150 base pair sequencing strategy (PE150). Sequencing data obtained from Illumina were transformed into raw sequence reads (raw data) using the CASAVA base recognition (base calling). The raw data were filtered for a cleaner downstream analysis. This was done by using the following exclusion criteria: adapter contamination, more than 10% of uncertain nucleotides

and more than 50% of low-quality nucleotides (base quality of <5). The library prepared from the filtered raw reads was then mapped to the reference genome Mus\_musculus\_Engsemble\_94 (GRCm38/mm10) using HISAT2. featureCounts was used to quantify the gene expression of the samples in terms of raw counts. Differential gene analysis was performed using the DESeq2 (v1.20.0) with threshold set as:  $|\log_2(\text{fold change})| \geq 1$  and  $\text{Padj} \leq 0.05$ . The statistical analysis of the differentially expressed genes was done using the following threshold parameter on DESeq2:  $P\text{ value} \leq 0.05$   $|\log_2(\text{fold change})| \geq 0.0$ . Fragments per kilobase of transcript per million mapped reads (FPKM) cluster analysis was performed for generating heatmaps, clustered using  $\log_2(\text{FPKM} + 1)$  value, with represented values ranging from +1.5 (red, high expression) to -1.5 (blue, low expression). For KEGG enrichment, analysis was performed using clusterProfiler (v3.8.1), with parameter set as:  $\text{Padj} < 0.05$ . A total of 12,710 gene transcripts were found to have significant differences in gene expression levels. On the basis of these data, Venn diagram, heatmaps, and KEGG pathway analysis were generated using Novogene software from Novogene.

### Enzyme-linked immunosorbent assay

Lung lysates of infected mice were prepared by mechanically homogenizing the lung explants in lysis buffer used for immunoblotting analyses. These lung protein lysates were then quantified for total protein amount using Bradford assay. Volumes of lysates having equal amounts of protein were used to quantify the IL-1 $\beta$  cytokines levels in the infected lung tissues. Enzyme-linked immunosorbent assay was performed using commercially available kits from R&D Systems (#DY401-05).

### Immunostaining

Mouse lungs were harvested and processed for immunostaining as described before (67). This was followed by incubation with a primary antibody, either conjugated with a fluorophore fluorescein isothiocyanate (FITC)-CD68 (BioLegend, #137006), FITC-Ly6G (CST, #88876), allophycocyanin (APC)-F4/80 (BioLegend, #157306), APC-CD80 (BioLegend, #104713), and APC-CD163 (BioLegend, #155305) or unconjugated p-NF- $\kappa$ B-p65 (Novus Biologicals, #NB-100 82088), CD3e (CST, #78588), and CD11c (CST, #97585). For p-p65 staining, the lung sections were washed with TBST (tris-buffered saline containing Tween 20) and incubated with Alexa Fluor 488 conjugated, anti-rabbit secondary antibody (Invitrogen #A32731). For staining CD3e and CD11c, lung sections were incubated with Alexa Fluor 488 conjugated, anti-rabbit secondary antibody (CST, #4412). The sections were further washed after incubation and mounted on glass slides using 4',6-diamidino-2-phenylindole (DAPI) Fluoromount-G (Southern Biotech, #0100-20). These were then either imaged using confocal microscopy, via Olympus VS120 Slide Scanner Slide Analyzer, and analyzed using Oly-Via (OLYMPUS OlyVIA 2.9) or imaged and analyzed using Zeiss Axio Imager.Z1 microscope and Zen blue (v3.7), respectively. H&E staining was performed as described previously (26, 67, 68).

### Macrophage enrichment assay

Whole lungs were isolated from infected mice and cut into small pieces in a DNase and collagenase (Thermo Fisher Scientific) containing buffer. These were then incubated in a 37°C rotor at 125 rpm for 30 min. After incubation, for further breakdown of the tissues, they were repeatedly flushed out using an 18-gauge syringe and passed through a 70- $\mu$ m prewetted filter. These cells were then centrifuged, and the pellet

was resuspended in MojoSort buffer (BioLegend, #480017) for cell counting. Equal number of cells isolated from each lung was then incubated with anti-F4/80 biotin-tagged antibody (BioLegend, #123105). After incubation with the primary antibody, the cells were centrifuged again, washed using the same buffer, resuspended, and incubated with magnetic MojoSort streptavidin nanobeads (BioLegend, #76447). After nanobead incubation, the cells were washed, resuspended, and then subjected to magnetic pulldown using a magnetic rack (Thermo Scientific MagJET rack, #MR02). This pull-down was repeated thrice to ensure the purity of the cell types. Supernatant collected at every stage was pooled, centrifuged, and used as controls. TRIzol was added to the pulled down beads after the third time and was processed for RNA extraction and qRT-PCR analyses.

### Flow cytometry

Whole lungs were isolated from infected animals and processed in the same way as for isolating single cells, as was done for the macrophage enrichment assay (above). Equal number of cells from each lung was then fixed using 4% paraformaldehyde (Electron Microscopy Sciences, #15714-S). After fixing, the cells were stained with conjugated primary antibodies, anti-mouse APC-CD80 (BioLegend, #104713) or APC-CD163 (BioLegend #155305). APC-Rat immunoglobulin G1 (BioLegend, #401904) was used as isotype control. Cell population positive for APC was acquired using BD FACSAria II flow cytometer, and data were analyzed using FlowJo.

### Quantification and statistical analyses

Quantification of band intensity in immunoblots was performed using the ImageJ for densitometric analyses. For quantification of H&E images, color deconvolution was performed using NIS viewer (v.5.21.00). ImageJ was then used to set the threshold, and watershed was applied to separate the closely spaced nuclei in the lung sections, followed by measuring the count of nuclei. Immunofluorescence images were also quantified using the ImageJ (69). Mean fluorescence intensity was measured for each protein along with their respective DAPI stains. These were then corrected for background, followed by which the fluorescent protein intensity for each field was normalized to its respective DAPI intensity. The resulting data are represented as mean fluorescence intensity. All statistical analyses were performed using GraphPad Prism 9 software and Microsoft Excel for Windows 10. Kaplan-Meier test was used to calculate the significance of survival. Two-tailed, unpaired Student's *t* test was performed to calculate statistical significance for two group comparisons. One-way analysis of variance (ANOVA) was used for calculating statistical significance of datasets having more than two groups. *P* < 0.05 was considered statistically significant.

### Supplementary Materials

This PDF file includes:

Figs. S1 to S7

Table S1

Original immunoblots for the panels presented in the manuscript

### REFERENCES AND NOTES

1. I. Astuti, Ysrafil, Severe acute respiratory syndrome coronavirus 2 (SARS-CoV-2): An overview of viral structure and host response. *Diabetes Metab. Syndr.* **14**, 407–412 (2020).
2. J. L. Casanova, L. Abel, Mechanisms of viral inflammation and disease in humans. *Science* **374**, 1080–1086 (2021).
3. X. J. Guo, P. G. Thomas, New fronts emerge in the influenza cytokine storm. *Semin. Immunopathol.* **39**, 541–550 (2017).
4. R. S. Peebles Jr., B. S. Graham, Pathogenesis of respiratory syncytial virus infection in the murine model. *Proc. Am. Thorac. Soc.* **2**, 110–115 (2005).
5. S. A. Taleb, A. A. Al Thani, K. Al Ansari, H. M. Yassine, Human respiratory syncytial virus: Pathogenesis, immune responses, and current vaccine approaches. *Eur. J. Clin. Microbiol. Infect. Dis.* **37**, 1817–1827 (2018).
6. A. Faist, J. Janowski, S. Kumar, S. Hinse, D. M. Caliskan, J. Lange, S. Ludwig, L. Brunotte, Virus infection and systemic inflammation: Lessons learnt from COVID-19 and beyond. *Cells* **11**, 2198 (2022).
7. Y. Gu, X. Zuo, S. Zhang, Z. Ouyang, S. Jiang, F. Wang, G. Wang, The mechanism behind influenza virus cytokine storm. *Viruses* **13**, 1362 (2021).
8. R. Karki, T. D. Kanneganti, Innate immunity, cytokine storm, and inflammatory cell death in COVID-19. *J. Transl. Med.* **20**, 542 (2022).
9. S. P. Nobis, M. Kopf, Tissue-resident macrophages: Guardians of organ homeostasis. *Trends Immunol.* **42**, 495–507 (2021).
10. A. H. Newton, A. Cardani, T. J. Bracie, The host immune response in respiratory virus infection: Balancing virus clearance and immunopathology. *Semin. Immunopathol.* **38**, 471–482 (2016).
11. J. Bernhagen, R. Krohn, H. Lue, J. L. Gregory, A. Zernecke, R. R. Koenen, M. Dewor, I. Georgiev, A. Schober, L. Leng, T. Kooistra, G. Fingerle-Rowson, P. Ghezzi, R. Kleemann, S. R. McColl, R. Bucala, M. J. Hickey, C. Weber, MIF is a noncognate ligand of CX3 chemokine receptors in inflammatory and atherosclerotic cell recruitment. *Nat. Med.* **13**, 587–596 (2007).
12. C. X. Foo, S. Bartlett, K. Y. Chew, M. D. Ngo, H. Bielefeldt-Ohmann, B. J. Arachchige, B. Matthews, S. Reed, R. Wang, C. Smith, M. J. Sweet, L. Burr, K. Bisht, S. Shatunova, J. E. Sinclair, R. Parry, Y. Yang, J. P. Levesque, A. Khromykh, M. M. Rosenkilde, K. R. Short, K. Ronacher, GPR183 antagonism reduces macrophage infiltration in influenza and SARS-CoV-2 infection. *Eur. Respir. J.* **61**, 2201306 (2023).
13. C. Xia, W. Xu, X. Ai, Y. Zhu, P. Geng, Y. Niu, H. Zhu, W. Zhou, H. Huang, X. Shi, Autophagy and exosome coordinately enhance macrophage M1 polarization and recruitment in influenza A virus infection. *Front. Immunol.* **13**, 722053 (2022).
14. V. Fensterl, S. Chattopadhyay, G. C. Sen, No love lost between viruses and interferons. *Annu. Rev. Virol.* **2**, 549–572 (2015).
15. M. S. Lee, Y. J. Kim, Signaling pathways downstream of pattern-recognition receptors and their cross talk. *Annu. Rev. Biochem.* **76**, 447–480 (2007).
16. T. Taniguchi, K. Ogasawara, A. Takaoka, N. Tanaka, IRF family of transcription factors as regulators of host defense. *Annu. Rev. Immunol.* **19**, 623–655 (2001).
17. J. Hiscott, Triggering the innate antiviral response through IRF-3 activation. *J. Biol. Chem.* **282**, 15325–15329 (2007).
18. F. Villalon-Letelier, A. G. Brooks, P. M. Saunders, S. L. Londrian, P. C. Reading, Host cell restriction factors that limit influenza A infection. *Viruses* **9**, 376 (2017).
19. L. Martin-Sancho, M. K. Lewinski, L. Pache, C. A. Stoneham, X. Yin, M. E. Becker, D. Pratt, C. Churas, S. B. Rosenthal, S. Liu, S. Weston, P. D. De Jesus, A. M. O'Neill, A. P. Gounder, C. Nguyen, Y. Pu, H. M. Curry, A. L. Oom, L. Miorin, A. Rodriguez-Frandsen, F. Zheng, C. Wu, Y. Xiong, M. Urbanowski, M. L. Shaw, M. W. Chang, C. Benner, T. J. Hope, M. B. Frieman, A. Garcia-Sastre, T. Ideker, J. F. Hultquist, J. Guatelli, S. K. Chanda, Functional landscape of SARS-CoV-2 cellular restriction. *Mol. Cell* **81**, 2656–2668.e8 (2021).
20. Y. Zhou, C. He, L. Wang, B. Ge, Post-translational regulation of antiviral innate signaling. *Eur. J. Immunol.* **47**, 1414–1426 (2017).
21. J. Hiscott, Convergence of the NF-κB and IRF pathways in the regulation of the innate antiviral response. *Cytokine Growth Factor Rev.* **18**, 483–490 (2007).
22. S. Chattopadhyay, T. Kuzmanovic, Y. Zhang, J. L. Wetzel, G. C. Sen, Ubiquitination of the transcription factor IRF-3 activates RIPA, the apoptotic pathway that protects mice from viral pathogenesis. *Immunity* **44**, 1151–1161 (2016).
23. S. Chattopadhyay, J. T. Marques, M. Yamashita, K. L. Peters, K. Smith, A. Desai, B. R. Williams, G. C. Sen, Viral apoptosis is induced by IRF-3-mediated activation of Bax. *EMBO J.* **29**, 1762–1773 (2010).
24. S. Chattopadhyay, M. Yamashita, Y. Zhang, G. C. Sen, The IRF-3/Bax-mediated apoptotic pathway, activated by viral cytoplasmic RNA and DNA, inhibits virus replication. *J. Virol.* **85**, 3708–3716 (2011).
25. S. Chakravarty, R. Chakravarti, S. Chattopadhyay, Inflammatory control of viral infection. *Viruses* **15**, 1579 (2023).
26. S. Popli, S. Chakravarty, S. Fan, A. Glanz, S. Aras, L. E. Nagy, G. C. Sen, R. Chakravarti, S. Chattopadhyay, IRF3 inhibits nuclear translocation of NF-κB to prevent viral inflammation. *Proc. Natl. Acad. Sci. U.S.A.* **119**, e2121385119 (2022).
27. S. Fan, S. Popli, S. Chakravarty, R. Chakravarti, S. Chattopadhyay, Non-transcriptional IRF7 interacts with NF-κB to inhibit viral inflammation. *J. Biol. Chem.* **300**, 107200 (2024).
28. R. W. Körner, M. Majjouti, M. A. A. Alcazar, E. Mahabir, Of mice and men: The coronavirus MHV and mouse models as a translational approach to understand SARS-CoV-2. *Viruses* **12**, 880 (2020).
29. Z. Yang, J. Du, G. Chen, J. Zhao, X. Yang, L. Su, G. Cheng, H. Tang, Coronavirus MHV-A59 infects the lung and causes severe pneumonia in C57BL/6 mice. *Virol. Sin.* **29**, 393–402 (2014).
30. J. Gao, Q. Wang, Y. D. Tang, J. Zhai, W. Hu, C. Zheng, When ferroptosis meets pathogenic infections. *Trends Microbiol.* **31**, 468–479 (2023).

31. L. Ghita, J. Spanier, C. Chhatbar, F. Mulenge, A. Pavlou, P. K. Larsen, I. Waltl, Y. Lueder, M. Kohls, K. Jung, S. M. Best, R. Forster, M. Stangel, D. Schreiner, U. Kalinke, MyD88 signaling by neurons induces chemokines that recruit protective leukocytes to the virus-infected CNS. *Sci. Immunol.* **6**, eabc9165 (2021).
32. C. E. Hughes, R. J. B. Nibbs, A guide to chemokines and their receptors. *FEBS J.* **285**, 2944–2971 (2018).
33. S. Tillmann, J. Bernhagen, H. Noels, Arrest functions of the MIF ligand/receptor axes in atherosclerosis. *Front. Immunol.* **4**, 115 (2013).
34. M. Ruiz Silva, H. van der Ende-Metselaar, H. L. Mulder, J. M. Smit, I. A. Rodenhuis-Zybert, Mechanism and role of MCP-1 upregulation upon chikungunya virus infection in human peripheral blood mononuclear cells. *Sci. Rep.* **6**, 32288 (2016).
35. R. Medzhitov, Inflammation 2010: New adventures of an old flame. *Cell* **140**, 771–776 (2010).
36. S. Chen, A. Saeed, Q. Liu, Q. Jiang, H. Xu, G. G. Xiao, L. Rao, Y. Duo, Macrophages in immunoregulation and therapeutics. *Signal Transduct. Target. Ther.* **8**, 207 (2023).
37. C. D. Mills, Anatomy of a discovery: M1 and M2 macrophages. *Front. Immunol.* **6**, 212 (2015).
38. R. Kumar, N. Khandelwal, R. Thachamvally, B. N. Tripathi, S. Barua, S. K. Kashyap, S. Mahendrani, N. Kumar, Role of MAPK/MNK1 signaling in virus replication. *Virus Res.* **253**, 48–61 (2018).
39. S. A. Barber, L. Bruett, B. R. Douglass, D. S. Herbst, M. C. Zink, J. E. Clements, Visna virus-induced activation of MAPK is required for virus replication and correlates with virus-induced neuropathology. *J. Virol.* **76**, 817–828 (2002).
40. L. Wang, Z. Xia, W. Tang, Y. Sun, Y. Wu, H. F. Kwok, F. Sun, Z. Cao, p38 activation and viral infection. *Expert Rev. Mol. Med.* **24**, e4 (2022).
41. Y. Cheng, F. Sun, L. Wang, M. Gao, Y. Xie, Y. Sun, H. Liu, Y. Yuan, W. Yi, Z. Huang, H. Yan, K. Peng, Y. Wu, Z. Cao, Virus-induced p38 MAPK activation facilitates viral infection. *Theranostics* **10**, 12223–12240 (2020).
42. L. M. Jenster, K. E. Lange, S. Normann, A. vom Hemdt, J. D. Wuerth, L. D. J. Schiffelers, Y. M. Tesfamariam, F. N. Gohr, L. Klein, I. H. Kalthueuner, S. Ebner, D. J. Lapp, J. Mayer, J. Moecking, H. L. Ploegh, E. Latz, F. Meissner, M. Geyer, B. M. Kummerer, F. I. Schmidt, P38 kinases mediate NLRP1 inflammasome activation after ribotoxic stress response and virus infection. *J. Exp. Med.* **220**, e20220837 (2023).
43. Y. Zhan, S. Yu, S. Yang, X. Qiu, C. Meng, L. Tan, C. Song, Y. Liao, W. Liu, Y. Sun, C. Ding, Newcastle Disease virus infection activates PI3K/Akt/mTOR and p38 MAPK/Mnk1 pathways to benefit viral mRNA translation via interaction of the viral NP protein and host eIF4E. *PLOS Pathog.* **16**, e1008610 (2020).
44. B. Bergstrom, I. B. Johnsen, T. T. Nguyen, L. Hagen, G. Slupphaug, L. Thommesen, M. W. Anthonson, Identification of a novel in vivo virus-targeted phosphorylation site in interferon regulatory factor-3 (IRF3). *J. Biol. Chem.* **285**, 24904–24914 (2010).
45. S. Chattopadhyay, M. Veleeparambil, D. Poddar, S. Abdulkhalek, S. K. Bandyopadhyay, V. Fensterl, G. C. Sen, EGFR kinase activity is required for TLR4 signaling and the septic shock response. *EMBO Rep.* **16**, 1535–1547 (2015).
46. A. M. Kell, M. Gale Jr., RIG-I in RNA virus recognition. *Virology* **479–480**, 110–121 (2015).
47. S. Chattopadhyay, G. C. Sen, RIG-I-like receptor-induced IRF3 mediated pathway of apoptosis (RIPA): A new antiviral pathway. *Protein Cell* **8**, 165–168 (2017).
48. A. Glanz, K. Chawla, S. Fabry, G. Subramanian, J. Garcia, B. Jay, J. Ciricillo, R. Chakravarti, R. T. Taylor, S. Chattopadhyay, High throughput screening of FDA-approved drug library reveals the compounds that promote IRF3-mediated pro-apoptotic pathway inhibit virus replication. *Viruses* **12**, 442 (2020).
49. J. L. Wetzel, V. Fensterl, G. C. Sen, Sendai virus pathogenesis in mice is prevented by Ifit2 and exacerbated by interferon. *J. Virol.* **88**, 13593–13601 (2014).
50. H. Yanai, S. Chiba, S. Hangai, K. Kometani, A. Inoue, Y. Kimura, T. Abe, H. Kiyonari, J. Nishio, N. Taguchi-Atarashi, Y. Mizushima, H. Negishi, R. Grosschedl, T. Taniguchi, Revisiting the role of IRF3 in inflammation and immunity by conditional and specifically targeted gene ablation in mice. *Proc. Natl. Acad. Sci. U.S.A.* **115**, 5253–5258 (2018).
51. S. Chattopadhyay, V. Fensterl, Y. Zhang, M. Veleeparambil, J. L. Wetzel, G. C. Sen, Inhibition of viral pathogenesis and promotion of the septic shock response to bacterial infection by IRF-3 are regulated by the acetylation and phosphorylation of its coactivators. *MBio* **4**, e00636-12 (2013).
52. E. G. Viox, T. N. Hoang, A. A. Upadhyay, R. Nchioua, M. Hirschenberger, Z. Strongin, G. K. Tharp, M. Pino, K. Nguyen, J. L. Harper, M. Gagne, S. Marciano, A. K. Boddapati, K. L. Pellegrini, A. Pradhan, J. Tisoncik-Go, L. S. Whitmore, K. A. Karunakaran, M. Roy, S. Kirejczyk, E. H. Curran, C. Wallace, J. S. Wood, F. Connor-Stroud, E. A. Voigt, C. M. Monaco, D. E. Gordon, S. P. Kasturi, R. D. Levitt, M. Gale Jr., T. H. Vanderford, G. Silvestri, K. Busman-Sahay, J. D. Estes, M. Vaccari, D. C. Douek, K. M. J. Sparre, R. P. Johnson, F. Kirchhoff, G. Schreiber, S. E. Bosingher, M. Paillardini, Modulation of type I interferon responses potentially inhibits SARS-CoV-2 replication and inflammation in rhesus macaques. *Sci. Immunol.* **8**, eadg0033 (2023).
53. S. Sakaguchi, H. Negishi, M. Asagiri, C. Nakajima, T. Mizutani, A. Takaoka, K. Honda, T. Taniguchi, Essential role of IRF-3 in lipopolysaccharide-induced interferon-beta gene expression and endotoxin shock. *Biochem. Biophys. Res. Commun.* **306**, 860–866 (2003).
54. S. J. Jenkins, D. Ruckerl, P. C. Cook, L. H. Jones, F. D. Finkelman, N. van Rooijen, A. S. MacDonald, J. E. Allen, Local macrophage proliferation, rather than recruitment from the blood, is a signature of TH2 inflammation. *Science* **332**, 1284–1288 (2011).
55. J. Shi, L. Hua, D. Harmer, P. Li, G. Ren, Cre driver mice targeting macrophages. *Methods Mol. Biol.* **1784**, 263–275 (2018).
56. K. Q. Gong, C. Frevert, A. M. Manicone, Deletion of LysM in LysMCre recombinase homozygous mice is non-contributory in LPS-induced acute lung injury. *Lung* **197**, 819–823 (2019).
57. B. E. Clausen, C. Burkhardt, W. Reith, R. Renkowitz, I. Förster, Conditional gene targeting in macrophages and granulocytes using LysMCre mice. *Transgenic Res.* **8**, 265–277 (1999).
58. L. Tarassishin, H. S. Suh, S. C. Lee, Interferon regulatory factor 3 plays an anti-inflammatory role in microglia by activating the PI3K/Akt pathway. *J. Neuroinflammation* **8**, 187 (2011).
59. J. L. McCaskill, S. Ressel, A. Alber, J. Redford, U. F. Power, J. Schwarze, B. M. Dutia, A. H. Buck, Broad-spectrum inhibition of respiratory virus infection by microRNA mimics targeting p38 MAPK signaling. *Mol. Ther. Nucleic Acids* **7**, 256–266 (2017).
60. M. Kandasamy, NF- $\kappa$ B signalling as a pharmacological target in COVID-19: Potential roles for IKK $\beta$  inhibitors. *Naunyn Schmiedebergs Arch. Pharmacol.* **394**, 561–567 (2021).
61. A. Costa, B. Sarmento, V. Seabra, Targeted drug delivery systems for lung macrophages. *Curr. Drug Targets* **16**, 1565–1581 (2015).
62. S. Arber Raviv, M. Alyan, E. Egorov, A. Zano, M. Y. Harush, C. Pieters, H. Korach-Rechtmann, A. Saadya, G. Kaneti, I. Nudelman, S. Farkash, O. D. Flikshtain, L. N. Mekies, L. Koren, Y. Gal, E. Dor, J. Shainsky, J. Shklover, Y. Adir, A. Schroeder, Lung targeted liposomes for treating ARDS. *J. Control. Release* **346**, 421–433 (2022).
63. H. Negishi, K. Matsuki, N. Endo, H. Sarashina, S. Miki, A. Matsuda, K. Fukazawa, N. Taguchi-Atarashi, H. Ikushima, H. Yanai, J. Nishio, K. Honda, Y. Fujioka, Y. Ohba, T. Noda, S. Taniguchi, E. Nishida, Y. Zhang, H. Chi, R. A. Flavell, T. Taniguchi, Beneficial innate signaling interference for antibacterial responses by a Toll-like receptor-mediated enhancement of the MKP-IRF3 axis. *Proc. Natl. Acad. Sci. U.S.A.* **110**, 19884–19889 (2013).
64. Y. Zhuang, M. Ortega-Ribera, P. Thevkar Nagesh, R. Joshi, H. Huang, Y. Wang, A. Zivny, J. Mehta, S. M. Parikh, G. Szabo, Bile acid-induced IRF3 phosphorylation mediates cell death, inflammatory responses, and fibrosis in cholestasis-induced liver and kidney injury via regulation of ZBP1. *Hepatology* **79**, 752–767 (2024).
65. J. Kim, J. V. Pena, H. P. McQueen, L. Kong, D. Michael, E. M. Lomashvili, P. R. Cook, Downstream STING pathways IRF3 and NF- $\kappa$ B differentially regulate CCL22 in response to cytosolic dsDNA. *Cancer Gene Ther.* **31**, 28–42 (2024).
66. J. H. Franco, R. A. Harris, W. G. Ryan, R. T. Taylor, R. E. McCullumsmith, S. Chattopadhyay, Z. K. Pan, Retinoic acid-mediated inhibition of mouse coronavirus replication is dependent on IRF3 and CaMKK. *Viruses* **16**, 140 (2024).
67. S. Chakravarty, G. Subramanian, S. Popli, M. Veleeparambil, S. Fan, R. Chakravarti, S. Chattopadhyay, Interferon-stimulated gene TDRD7 interacts with AMPK and inhibits its activation to suppress viral replication and pathogenesis. *MBio* **14**, e0061123 (2023).
68. J. Kim, K. Chun, J. McGowan, Y. Zhang, P. J. Czernik, B. Mell, B. Joe, S. Chattopadhyay, J. Holoshitz, R. Chakravarti, 14-3-3 $\zeta$ : A suppressor of inflammatory arthritis. *Proc. Natl. Acad. Sci. U.S.A.* **118**, e2025257118 (2021).
69. M. H. Shihani, S. G. Novo, S. J. Le Marchand, Y. Wang, M. K. Duncan, A simple method for quantitating confocal fluorescent images. *Biochem. Biophys. Rep.* **25**, 100916 (2021).

**Acknowledgments:** We thank G. Sen for providing the *Irif3-f1* mice, K. Pan, R. Worth, and M. Vijay-Kumar for input on the study and J. Kim and R. Harris for technical assistance. The following reagents were obtained through BEI Resources, National Institute of Allergy and Infectious Diseases, NIH: recombinant murine coronavirus strain iCA59 (NR-43000) and mouse macrophage WT cell line (NR-9456). **Funding:** This work was supported partly by the National Institutes of Health grants AI155545 (to S.Chak.), AI165521 (to S.Chak.), AA027456 (to S.Chak.), AI153496 (to R.T.T.), and AI184880 (to R.C.) and the American Heart Association pre-doctoral fellowship 1019592 (to S.Chak.). **Author contributions:** S.Chak.:Writing—original draft, conceptualization, investigation, writing—review and editing, methodology, resources, funding acquisition, data curation, validation, supervision, formal analysis, project administration, and visualization. M.V.: Writing—original draft, investigation, writing—review and editing, validation, formal analysis, and visualization. S.F.: Investigation, resources, validation, formal analysis, and visualization. R.T.T.: Conceptualization, methodology, resources, funding acquisition, supervision, and project administration. R.C.: Conceptualization, writing—review and editing, methodology, resources, and supervision. S.Chak.: Writing—original draft, conceptualization, investigation, writing—review and editing, methodology, resources, funding acquisition, data curation, validation, supervision, formal analysis, project administration, and visualization. **Competing interests:** The authors declare that they have no competing interests. **Data and materials availability:** The RNA-seq data have been uploaded into GEO (accession number GSE267631). Mice generated in the study may be provided by S.Chak. All other data needed to evaluate the conclusions in the paper are present in the paper and/or the Supplementary Materials.

Submitted 5 December 2023

Accepted 5 July 2024

Published 9 August 2024

10.1126/sciadv.adn2858